Physical Properties That Determine The resolution limit of planar Hall Effect Sensors

Vladislav Mor

Department of Physics

Ph.D. Thesis

Submitted to the Senate of Bar-Ilan University

Ramat-Gan, Israel December 2015

This work was carried out under the supervision of

Professor Lior Klein

Department of Physics

Bar-Ilan University

Acknowledgments

The years of my study were a wonderful educational period that provided me the opportunity to be involved in scientific research. Many scientists, some of whom became my friends, enabled me to add my humble contribution to several works in the fields of physics and chemistry and Engineering. To the good people that taught me and worked with me I would like to express my acknowledgements.

First, I would like to thank my advisor, Prof. Lior Klein, who introduced me into experimental solid state physics, gave me an opportunity to be involved in every aspect of a research work, and allowed me to test some of my ideas freely. I much appreciate his great dedication to his students and his advice.

I want to thank prof. Yuval Garini the head of Bar Ilan institute for Nanotechnology and Advanced Materials.

I thank my dear friends Dr. Moty Schultz Dr. Debangsu Roy and Dr. Omer Sinwani who collaborated with me in sensors project.

I want to thank several members from the Physics department: Prof. Aviad Frydman, Prof. Amos Sharoni, Prof. Leonid Feigal, Prof. Yitzhak Rabin, Prof. Michael Rozenbluh, Dr. Yuri Kaganovskii.

I want to thank several members from the chemistry department at Bar-Ilan University: Prof. Daniel Nessim, Efrat Shaoat, Merav Muallem and Dr. Eti Teblum.

I had the honor to work and study with Asaf Grosz, Dr. Ilya Sochnikov, Nathan Chejanovsky, Elhanan Blaut, Keren

Shemesh, Dr. Ran Califa, Omri Sharon, Lior Shani, Dr.Tal Havdala, Ted Frumkin, Dr. Rafi Vered, Ilia Raysin.

I would like to thank Dr. Yossi Abulafia - Head of Nano-Fabrication Unit, Dr. Olga Girshevitz - Head of Surface Analysis Facility, Moshe Feldberg - Head of Clean room facilities, Gili Chen-Taguri - Head of XRD Unit, Dr. Yosef Tal-Yosef – Head of HR-SEM Unit amd Mark Oksman.

I also thank the secretaries of the department of physics, Rita Golender, Ortal Mizrahi Rachel Rotberg and Sara Bialkovitch, that always found time help me in any way they could. I thank Dr. Efrat Bodner and the late Dr. Orit Chasid who made all the bureaucratically arrangements concerning my work as scientific equipment operator.

It has been a great pleasure for me to share the lab with Dr. Yevgeniy Telepinsky, Dr. Moty Schultz, Dr. Debangsu Roy, Dr. Nati Naftalis, Dr. Yishai shperber, Dr. Snir Seri, Dr. Isaschar Genish, Dr. Noam Haham, Dr. Omer Sinwani, Livnat Landau, Pavel Tikhonov, Avi Yablonovich, Sagi Davidovich, Avishay Shapira, Stas Sorokin...

Finally, I want to thank my family: My parents for their support. Last but not least I would like thank my wonderful wife Anat, my source of joy, who helped me and supported me over the years.

Table of Contents:

Abstract

In the present era, sensitive magnetic field sensors are an integral part of our daily life: they are used to read magnetic data storage devices, for detecting variation of the Earth magnetic field which is useful for navigation or for detecting objects containing magnetic materials, for voltage and frequency shift sensing, MRI etc. Among the different types of magnetic sensors, magnetoresistive sensors are particularly interesting due to a combination of low cost and high sensitivity. For this reason they are widely used in many areas of technology and industry as well as in our daily lives. Nevertheless, there are still important areas such as medical application and certain defense applications for which the current sensitivity of magnetoresistive sensors is insufficient. For this reason finding new ways to fabricate a relatively cheap, simple, small magnetoresistive sensor that will also operate at room temperature is an important goal.

In this thesis, we demonstrate the prospects of ultra-sensitive magnetic field sensors that are based on Planar Hall Effect (PHE) in Permalloy (Py) films. The sensor described in this work utilizes the shape induced magnetic anisotropy of ferromagnetic layers and it is optimized to obtain large signal and low noise. Consequently, its field resolution is an order of magnitude higher than any other reported PHE sensor. Furthermore, at low frequencies it is more sensitive than any known commercial magnetoresistive sensor.

The first article "Planar Hall effect sensors with shape-induced effective single domain behavior" [I] presents a

comprehensive study of shape-induced magnetic anisotropy in patterned permalloy thin films in the form of elongated ellipses. We studied a wide range of sizes for the ellipse: from micrometer scale to millimeter scale. We showed that shape anisotropy can be reliably used for achieving effective single domain behavior. This phenomenon exists even in ellipses with major axis on the order of millimeters, provided the axes ratio of the ellipses is large enough. We also showed that shape induced anisotropy can be approximated analytically. In addition to the analytical model, we have carried out numerical simulations using OOMMF software. The simulations indicated the effective single domain behavior for ellipsoids and ellipses in a very wide range of sizes, whereas rectangular samples are less stable. These studies open the door for using such ellipses as the central part of a PHE magnetic sensor.

The second article "Planar Hall Effect Sensors with Subnanotesla Resolution" [II] presents the noise model of the sensor. We were able to identify the factors affecting the resolution and we have developed a model that allows to design a sensor with optimal resolution field. Our model takes into account various sources of noise: amplifier noise, thermal noise and $1/f$ noise. To develop PHE sensors with improved resolution, we took the following approach: (a) we used an AC excitation current to translate the sensor output signal to frequencies where the $1/f$ noise of the electronic preamplifier can be neglected, (b) guided by an analytical model, we optimized the thickness of the magnetic layer, and (c) we optimized the amplitude of the excitation current, (d) we

decrease the anisotropy field in order to increase the sensitivity of the sensor. The optimization process yielded exceptional field resolution: 600 $^{pT}/_{\sqrt{Hz}}$.

The third article "Composed planar Hall effect sensors with dual-mode operation" [III] discusses a possible application: a device that combines sensing and memory features. We presented a composed planar Hall effect sensor (CPHES) with two modes of operation. The CPHES is based on a pair of elongated magnetic ellipses made of Permalloy, and the PHE response is measured across the two ellipses. Parallel magnetization alignment in the two ellipses, corresponding to an ON mode, yields a PHE response similar to a response of a single PHE ellipse, while antiparallel magnetization alignment, corresponding to an OFF mode, yields a negligible response. We showed switchings between OFF and ON modes of a CPHES triggered by magnetic field. The CPHES can be useful for a variety of applications. It can be used as a switch triggered by magnetic field. It can be used as a marker which indicates exposure to a magnetic field exceeding a certain threshold without the need to constantly monitor the magnetic field. The novelty of the design allows the user to tailor the activation field by selecting of axes ratio of the ellipses.

In addition to the main study outlined above, we were able to make an important contribution to the study related to Planar Hall Effect based magnetic random access memory (MRAM). Three articles on this topic are presented in the Publications section [VI-VIII]. In addition, we have

collaborated with a group in the Department of Chemistry in studying carbon nanotubes (CNT) [IX].

In summary, the main achievement of our study is the development of an ultra-sensitive magnetic sensor based on the PHE which is more than an order of magnitude more sensitive than any other PHE sensor and is more sensitive at low frequencies than any known commercial magnetoresistive sensor. This achievement opens the door for many future applications in various fields including military and medical applications.

We attribute the exceptional sensitivity of our sensors to several factors: (a) studying and developing the use of shape anisotropy for inducing magnetic anisotropy and applying it to determine the shape of the magnetic sensor (b) developing a noise model and using it for optimization the sensor dimensions (c) optimizing the fabrication process including film growth and patterning.

Based on our present understanding of the important factors that determine the sensor sensitivity, we are confident that the field resolution can be further improved by at least another order of magnitude, which will make our sensors even more attractive for applications. In particular, we are pleased to report that there are now attempts in our group to develop a lab-on-a-chip system designed to detect very small concentrations of specific proteins in a solution. The detection method is based on using magnetic sensors to detect the

hydrodynamic properties of magnetic nanoparticles coated for binding to the specific proteins, as the Brownian motion of the nanoparticles changes when proteins bind to them. We believe that this is only the beginning and more applications will emerge with further improvement of the sensors.

Publications.

I. *Planar Hall effect sensors with shape-induced effective single domain behavior*. V. Mor, M. Shults, O. Sinwani, A. Grosz E. Paperno and L. Klein; J. appl. Phys., 111, 07E519, (2011).

II. *Planar Hall Effect Sensors With Subnanotesla Resolution*. A. Grosz, V. Mor, E. Paperno, S. Amrusi, I. Favilov, M. Shults and L. Klein; IEEE MAGNETICS LETTERS, 4, (2013).

III. *Composed planar Hall effect sensors with dual-modeoperation*. V. Mor, D. Roy, M. Schultz and L. Klein. AIP Advances, 6, 2, 025302, (2016).

IV. *Shape-induced bi-stable magnetic states in submicrometer structures of permalloy films*. Y. Telepinsky, V.. Mor, M. Schultz and L. Klein; J. Appl. Phys. 111, 07C715, (2012).

V. *A High-Resolution Planar Hall Effect Magnetometer for Ultra-Low Frequencies*. A. Grosz, V. Mor, S. Amrusi, I. Faivinov, E. Paperno, and L. Klein; IEEE Sensors Journal, 16, 9, 3224, (2016).

VI. *Planar Hall Effect Magnetometers*. V. Mor, A. Grosz, and L. Klein. High Sensitivity Magnetometers. Springer International Publishing Switzerland (2016).

VII. *Towards a six-state magnetic memory element*. Y. Telepinsky, V. Mor, M. Schultz, Yu-Ming Hung, A. D. Kent, and L. Klein; Applied Physics Letters, 105, 18, 182401, (2016).

VIII. *Magnetic thermal stability of Permalloy microstructures with shape-induced bi-axial anisotropy.*
Y. Telepinsky, O. Sinwani, V. Mor, M. Schultz, and L. Klein. J. Appl. Phys. 119, 8, 083902, (2016)

IX. *What is below the support layer affects carbonnanotube growth: an iron catalyst reservoir yields taller nanotube carpets***.** E. Shawat, V. Mor, L. Oakes, Y. Fleger, C. L. Pint and G. D. Nessim; Nanoscale, 6, 1545, (2014).

1. Scientific Background.

1.1 Introduction.

This chapter deals with the basics of ferromagnetism, magnetoresistance effects, spintronics, magnetic anisotropy and magnetization reversal. The chapter is divided into four sections:

1. The first section provides an overview of itinerant magnetism.
2. The second section starts with an overview of main magnetoresistance effects which includes:
    a. Anisotropic Magnetoresistance (AMR).
    b. Planar Hall Effect (PHE).
    c. GMR and TMR,

and describe the present status of the field of spintronics.

3. The third section introduces different types of magnetic anisotropy such as:
    a. Magnetocrystaline Anisotropy.
    b. Field-induced Anisotropy.
    c. Exchange-induced anisotropy.
    d. Shape-induced Anisotropy.
4. The last section describes the different magnetization reversal processes:
    a. Nucleation.
    b. Single domain reversal.

1.2 Itinerant Magnetism.

Itinerant ferromagnetism is ferromagnetism of conductors which arises from spontaneous spin splitting of bands which also populate the Fermi surface. As a result, charge carriers associated with the magnetization also contribute to the conduction. Furthermore, the spin-up carriers and the spin-down carriers frequently have different densities at the Fermi surface and hence charge current is also associated with a net flow of spins. In the following section, we present the Stoner criteria for spontaneous spin splitting of the energy bands.

The exchange energy describes an interaction between two neighboring spins and is given by

$$E_{ex} = -2J_{ex}S_i \cdot S_j, \tag{1.1}$$

where J_{ex} is the exchange integral, and S_i, S_j are the spins at atom i and atom j. If one assumes that the average spin is $\langle S \rangle$ then the exchange energy between a certain spin with the surrounding neighbors, ignoring long-range interactions, can be written as

$$E_{ex\_i} \sim -2J_{ex}\langle S \rangle (S_{\uparrow}\langle Z_{\uparrow} \rangle + S_{\downarrow}\langle Z_{\downarrow} \rangle), \tag{1.2}$$

where $\langle Z_{\uparrow} \rangle$ and $\langle Z_{\downarrow} \rangle$ are the average number of surrounding neighbors with spin up ($\uparrow$) and down ($\downarrow$), respectively. Therefore, the total gain in exchange energy due to a spin splitting process can be approximated as

$$\Delta E_{ex} \sim -zNJ_{ex}S^2m^2, \tag{1.3}$$

where m is the number of unbalanced spins per atom, z is the number of neighboring spins and N is the number of atoms. When the system gains energy from the exchange interaction considering positive J_{ex}, the kinetic energy of half of the unpaired spins increases by δE: $\Delta E_k \sim \frac{1}{2}Nm\delta E$.

The number of unbalanced spins, Nm, is equal to the number of electrons in the Fermi level, and is given by $Nm = \mathrm{g}(E_F)(\delta E)$ where $\mathrm{g}(E_F)$ is the density of states at the Fermi level (Figure 1).

The total change in energy during a spin splitting process is:

$$\Delta E_{ex} \sim \frac{1}{2\mathrm{g}(E_F)}N^2m^2 - zNJ_{ex}S^2m^2. \tag{1.4}$$

In order to obtain itinerant ferromagnetism in a material, this expression must be negative, in other words, the gain in exchange energy should be higher than the cost of the kinetic energy. This condition leads to the Stoner criterion for ferromagnetism [1, 2]:

$$1 < \frac{\mathrm{g}(E_F)}{N}2zS^2J_{ex}. \tag{1.5}$$

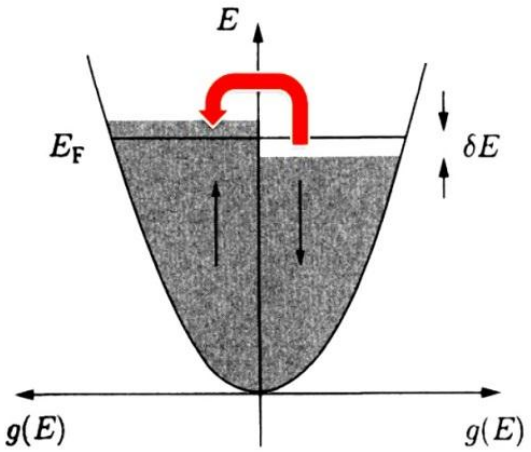

Figure 1.1 The density of states g as a function of the energy E, for spin up (↑) and spin down (↓). The red arrow represents flipping of $\frac{1}{2}Nm$ spins.

1.3 Magnetoresistance Effect, Spintonics.

1.3.1 Anisotropic Magnetoresistance (AMR).

Anisotropic magnetoresistance (AMR) in ferromagnetic conductors is the dependence of the electrical resistivity on the angle between the current $\vec{\mathbf{J}}$ direction, and the magnetization $\vec{\mathbf{M}}$ orientation. The AMR is a spin-orbit effect [3]; however, the specific mechanism is system dependent. AMR was studied extensively for more than a century and it was used in various commercial devices including data recording devices and magnetic sensors. The fact that the resistivity depends on the orientation of the measurement configuration relative to the current, means that one must use a resistivity tensor. In isotropic materials the relation between the electric field and the current density is given by Ohm's law:

$$\vec{\mathbf{E}} = \rho\vec{\mathbf{J}}, \tag{1.6}$$

In general, for two dimensional cases ρ is a tensor, and for a material that exhibits AMR it is given by:

$$\rho = \begin{pmatrix} \rho_{\parallel} & \\ & \rho_{\perp} \end{pmatrix}, \tag{1.7}$$

where $\rho_{\parallel}$ and $\rho_{\perp}$ are the resistivities for the currents parallel and perpendicular to the magnetization, respectively. Defining $\hat{u} = \langle \cos\theta, \sin\theta \rangle$ as a unit vector in the direction of the current $\vec{\mathbf{J}}$, (θ is the angle between $\vec{\mathbf{J}}$ and $\vec{\mathbf{M}}$), the longitudinal resistivity (measured in the $\vec{J}$ direction) can be expressed as:

$$\rho_{long} = \frac{\vec{E} \cdot \hat{u}}{|\vec{J}|}, \tag{1.9}$$

By substituting equation 1.6 into equation 1.9 we obtain:

$$\rho_{long} = \frac{\vec{u} \rho \vec{J}}{|\vec{J}|} = \hat{u} \rho \hat{u}^{T}, \tag{1.10}$$

and finally:

$$\rho_{long} = \rho_{\perp} + (\rho_{\parallel} - \rho_{\perp} \cos^2\theta) \ , \tag{1.11}$$

The AMR effect is defined as the ratio

$$AMR = \frac{\rho_{\parallel} - \rho_{\perp}}{\rho_{ev}} \ , \tag{1.12}$$

where $\rho_{ev} = \frac{1}{3}\rho_{\parallel} + \frac{2}{3}\rho_{\perp}$.

In materials like permalloy, NiCo alloys etc. (depending on film preparation method, substrate, capping layer) the

typical AMR values are 1-5% in permalloy [3-7] and 1-6% in NiCo alloys [3]. In ferromagnetic thin layers, AMR ratio increases with increasing film thickness and reaches a saturation value that is detected in bulk samples. There are two effects that may explain this. First, the thin films may be structurally less well defined than bulk specimen and additional electron scattering at grains and various defects can be observed. Second, diffusive scattering at the outer boundaries of the film may affect the AMR ratio [8].

1.3.1 Planar Hall Effect.

The resistivity tensor yields also a transverse effect. Defining a unit vector perpendicular to the current direction, $\hat{v} = \langle -\sin\theta, \cos\theta \rangle$ we can extract the transverse resistivity ρ_{trans}:

$$\rho_{trans} = \frac{\vec{E}\cdot\hat{v}}{|\vec{J}|}, \tag{1.13}$$

Substituting equation 6 in equation 13 yields:

$$\rho_{trans} = \frac{\vec{v}\rho\vec{J}}{|\vec{J}|} = \hat{v}\rho\hat{u}^T, \tag{1.14}$$

and finally:

$$\rho_{trans} = \frac{1}{2}(\rho_{\parallel} - \rho_{\perp})\sin\theta\cos\theta, \tag{1.15}$$

This transverse resistivity is called planar Hall effect (PHE) and contrary to the ordinary Hall Effect (OHE) it is symmetric under magnetic inversion. The PHE in magnetic

materials has been used so far mainly in 3d ferromagnetic layers and multilayers as a tool for measuring in-plane magnetization [9]. In addition, there have also been suggestions to use it for low field magnetic sensors [9-13].

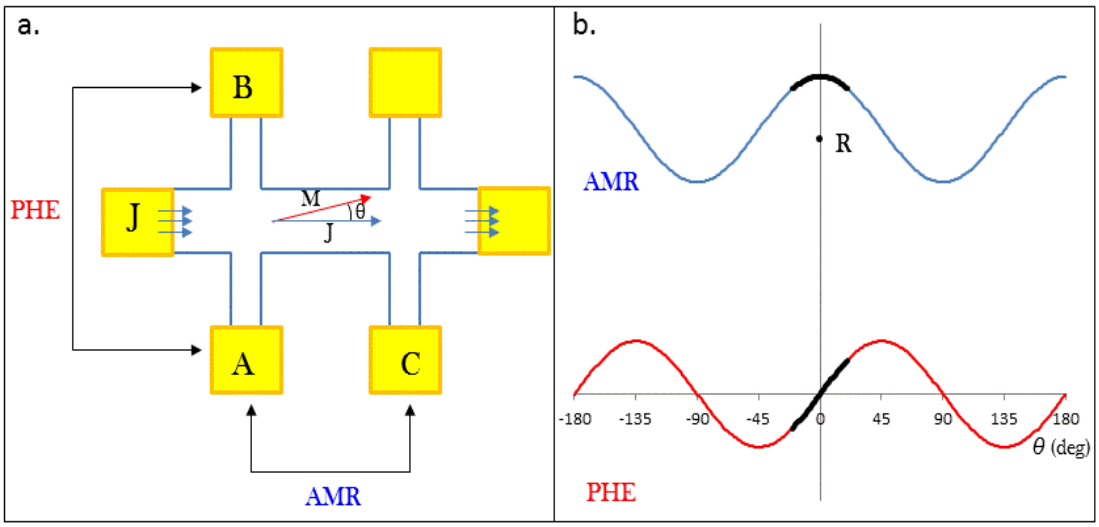

Figure 1.2 a) A sketch of a typical pattern used for measuring AMR and PHE. b) The dependence of the longitudinal and transverse resistance on the angle θ between the current J and the magnetization M demonstrating AMR (blue graph) and PHE (red graph), respectively.

1.3.2 GMR and TMR.

Giant magnetoresistance (GMR) is one of the most fascinating discoveries in thin-film magnetism, which combines both tremendous technological potential and deep fundamental physics. Within a decade after the discovery of GMR in 1988 [14, 15] commercial devices exploiting this phenomenon, such as hard-disk read-heads, magnetic field sensors and magnetic memory chips, become available in the market.

GMR can be qualitatively understood using the Mott model, which was introduced to explain the sudden increase in resistivity of ferromagnetic metals as they are heated above the

Curie temperature [16, 17]. There are two main points proposed by Mott. First, the electrical conductivity in metals can be represented as two largely independent conducting channels, corresponding to the up-spin and down-spin electrons, which are distinguished according to the projection of their spins along the quantization axis. The probability of spin-flip scattering processes in metals is usually small compared to the probability of the scattering processes in which the spin is conserved. This implies that the up-spin and down-spin electrons do not mix over long distances and, consequently, the electrical conduction occurs in parallel for the two spin channels. Commonly, the scattering rates of the up-spin and down-spin electrons are quite different.

According to Mott, the electric current is primarily carried by electrons from the valence *sp* bands due to their low effective mass and high mobility. The *d* bands play an important role in providing final states for the scattering of the *sp* electrons. In ferromagnets the *d* bands are exchange-split, so that the density of states is not the same for the up-spin and down-spin electrons at the Fermi energy. The probability of scattering into these states is proportional to their density, so that the scattering rates are spin-dependent, i.e. are different for the two conduction channels.

Using Mott's arguments it is straightforward to explain GMR in magnetic multilayers. One can consider collinear magnetic configurations, as is shown in Figure 1.3, and assume that the scattering is strong for electrons with spin antiparallel to the magnetization direction, and is weak for electrons with spin parallel to the magnetization direction. For the parallel-

aligned magnetic layers (the top panel in Figure.1.3a), the up-spin electrons pass through the structure almost without scattering, because their spin is parallel to the magnetization of the layers. On the other hand, the down-spin electrons are scattered strongly within both ferromagnetic layers, because their spin is antiparallel to the magnetization of the layers. Since conduction occurs in parallel for the two spin channels, the total resistivity of the multilayer is determined mainly by the highly-conductive up-spin electrons and appears to be low. For the antiparallel-aligned multilayer (the top panel in Figure 1.3b), both the up-spin and down-spin electrons are scattered strongly within one of the ferromagnetic layers, because within one of the layers the spin is antiparallel to the magnetization direction. Therefore, in this case the total resistivity of the multilayer is higher [18].

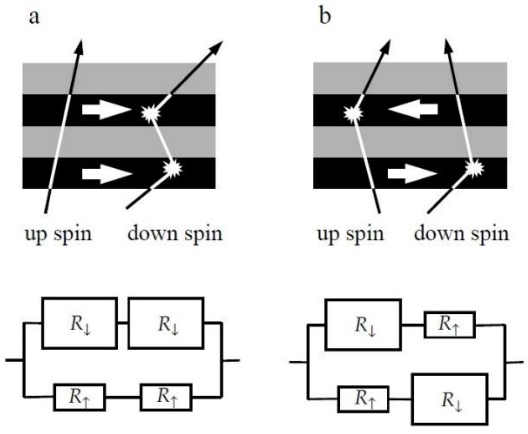

Figure 1.3 Schematic illustration of electron transport in a multilayer for parallel (a) and antiparallel (b) magnetizations of the successive ferromagnetic layers. The magnetization directions are specified by the arrows. The solid lines are individual electron trajectories within the two pin channels. The mean free path is much longer than the layer thicknesses and the net electric current flows in the plane of the layers. Bottom panels show the effective resistor network within the two-current series resistor model. For the parallel-aligned multilayer (a), the up-spin electrons pass through the structure almost without scattering, whereas the down-spin electrons are scattered strongly within both ferromagnetic layers. Since conduction occurs in parallel for the two spin channels, the total resistivity of the

multilayer is low. For the antiparallel-aligned multilayer (b), both the up-spin and downspin electrons are scattered strongly within one of the ferromagnetic layers, and the total resistivity of the multilayer is high.

When the two ferromagnetic layers are separated by an insulating layer, the effect is called Tunneling Magneto Resistance (TMR) [19-22]. The tunneling resistance depends even more strongly on the relative orientation of the ferromagnetic films.

Electric current can be passed through magnetic superlattices in two ways. In the current in plane (CIP) geometry, the current flows along the layers and the electrodes are located on one side of the structure. In the current perpendicular to plane (CPP) configuration, the current is passed perpendicular to the layers, and the electrodes are located on different sides of the superlattice [23]. The CPP geometry results in more than twice higher GMR, but is more difficult to realize in practice than the CIP configuration [24].

1.4 Magnetic Anisotropy.

Magnetization in a ferromagnetic material prefers to align its spins along a particular direction and this phenomenon is known as magnetic anisotropy. The preferred directions are called the easy axes of the magnetization. In the simplest case involving a single easy axis in the magnetic materials, the magnetic anisotropy energy is described by:

$$H = K_u \sin^2 \theta, \tag{1.16}$$

where K_u is the magnetic anisotropy constant and θ is the angle between the magnetization and the easy axis (EA) direction. In

the absence of an external magnetic field, the magnetization in a ferromagnetic material would be along one of the easy axes of the magnetization. In order to flip the magnetization direction when the spins are aligned along one of the easy axes, one needs to apply an external field in the opposite direction sufficient enough to circumvent the magnetic anisotropy energy. Magnetic anisotropy has four main sources: magnetocrystalline anisotropy, field induced anisotropy, Exchange-induced anisotropy and Shape induced Anisotropy.

1.4.1 Magnetocrystalline Anisotropy.

Magnetization measurements of magnetic crystals indicate that we need to apply different magnetic fields to magnetize the material in different directions. The preferred magnetization direction(s) is called the ***easy axis*** (or axes) of magnetization. A magnetic crystal with a single magnetic easy axis is called a uniaxial magnetic material and the corresponding anisotropy is named uniaxial magnetocrystalline anisotropy.

In this system, the crystal energy is usually can be expressed as a sum of power series

$$E = K_{u0} + K_{u1} \sin^2 \theta + K_{u2} \sin^4 \theta + \cdots, \qquad (1.17)$$

where K_{uj} is the anisotropy constant, and θ is the angle between the magnetization and the easy axis.

1.4.2 Field induced Anisotropy.

When certain alloys are heat treated in presence of a magnetic field and then cooled to room temperature, they develop a

uniaxial anisotropy with the easy axis parallel to the direction of the magnetic field applied during heat treatment. The rearrangement of atoms in the local scale is the reason behind the occurrence of this anisotropy.

At an annealing temperature T_a sufficiently high for atomic mobility, yet not so high that the material would lose its magnetic properties ($T_a < T_c$), some atom pairs orient themselves relative to the direction of applied field in order to reduce its magnetic anisotropy energy. Once the temperature is reduced to a level at which significant diffusion is no longer possible; the external field is removed. After the removal of the external magnetic field, the frozen-in atomic pair directional ordering persists. This may be sufficient to overcome the other anisotropies and could act as a preferred direction for the magnetization defined by the direction of the external applied field during annealing [25]. The field must be sufficiently large to saturate the specimen during magnetic anneal. Usually a field of few Oersteds is enough, since the material is magnetically soft to begin with, and its permeability at the magnetic annealing temperature is higher than at room temperature. The expression “magnetic annealing” is applied both to the treatment itself and to the phenomenon which occurs during the treatment [2, 26].

1.4.3 Exchange-induced anisotropy.

The usage of Exchange-induced anisotropy is a powerful technique for modifying and controlling magnetic

characteristics based on the use of magnetic heterostructures with properties governed by the interface region.

One of the most interesting interfaces for basic study and application is the interface between a ferromagnet and an antiferromagnet. A ferromagnet, such as iron, has a large exchange parameter but a relatively small anisotropy. This makes ferromagnetic order stable at high temperatures however the same is not true for its orientation particularly if the dimensions are a few nanometers. Many antiferromagnets have large anisotropies and consequently very stable orientations. In heterostructures, exchange coupling between the ferromagnet and antiferromagnets can, in principle, produce a ferromagnetic behavior with stable order and high anisotropy [27]. In such a structure, the anisotropy may behave as uniaxial. This phenomenon is called exchange bias because the hysteresis loop associated with the ferromagnet/antiferromagnet structure can be centered about a non-zero magnetic field.

1.4.4 Shape induced Anisotropy.

Magnetic anisotropy which depends on the sample's geometrical factors is called shape anisotropy. In a sample without magnetocrystalline anisotropy (e.g., amorphous or polycrystalline magnetic alloys), shape anisotropy determines the preferred direction of magnetization. The source of shape anisotropy is the demagnetization field H_d which is opposite to the samples magnetization. The magnetic induction field can be written as:

$$B = -H_d + 4\pi M \ , \tag{1.18}$$

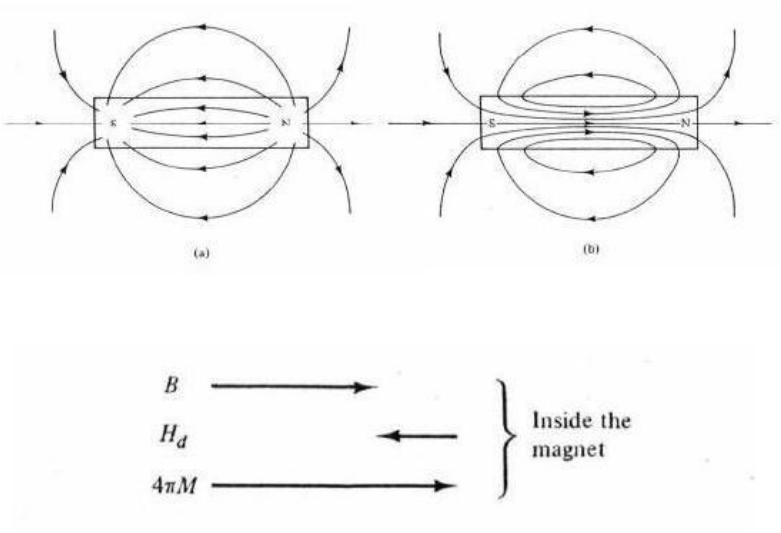

Figure 1.4 Fields of a bar magnet in Zero applied field after magnetizing it with an external field: (a) **H** field, and (b) **B** field. The vectors in the center indicate the values of these quantities at the center of the magnet [2].

where H_d is the demagnetization field (the value of H_d never exceeds $4\pi M$) and **M** is the magnetization (Figure 1.4). The demagnetization field is proportional to the magnetization with a pre-factor of N_d which depends on the sample's shape

$$H_d = N_d M, \tag{1.19}$$

The equations in the following sections are for the demagnetizing factors along the three axes of a general ellipsoid assuming that

$$a \geq b \geq c, \tag{1.20}$$

where a, b and c are the ellipsoid's semi-axes. The demagnetizing factors (corresponding to the semi-axes a, b and c) are labeled as N_a, N_b and N_c [28]. The formulae for N_a, N_b and N_c are:

$$N_a/_{4\pi} = \frac{\cos\varphi\cos\theta}{\sin^3\theta\sin^2\alpha}[F(k,\theta) - E(k,\theta)]\ , \tag{1.21}$$

$$N_b/_{4\pi} = \frac{\cos\varphi\cos\theta}{\sin^3\theta\sin^2\alpha\, cos^2\alpha}\Big[E(k,\theta) - cos^2\alpha\, F(k,\theta) - \frac{\sin^2\alpha\sin\theta\cos\theta}{\cos\varphi}\Big]\ , \tag{1.22}$$

$$N_c/_{4\pi} = \frac{\cos\varphi\cos\theta}{\sin^3\theta\, cos^2\alpha}\Big[\frac{\sin\theta\cos\varphi}{\cos\theta} - E(k,\theta)\Big]\ , \tag{1.23}$$

where

$$\cos\theta = c/a \qquad 0 \leq \theta \leq \pi/2 \tag{1.24}$$

$$\cos\varphi = b/a \qquad 0 \leq \varphi \leq \pi/2 \tag{1.25}$$

$$\sin\alpha = \left[\frac{1-(b/a)^2}{1-(c/a)^2}\right]^{\frac{1}{2}} = \frac{\sin\varphi}{\sin\theta} = k \qquad 0 \leq \alpha \leq \pi/2 \tag{1.26}$$

and $F(k,\theta)$ and $E(k,\theta)$ are incomplete elliptic integrals of the first and second kinds:

$$F(k,\theta) = \int_0^\theta \frac{d\phi}{\sqrt{1-k^2\sin^2\phi}}, \tag{1.27}$$

$$E(k,\theta) = \int_0^\theta \sqrt{1-k^2\sin^2\phi}\, d\phi, \tag{1.28}$$

k is the modulus and θ is the amplitude of these integrals.

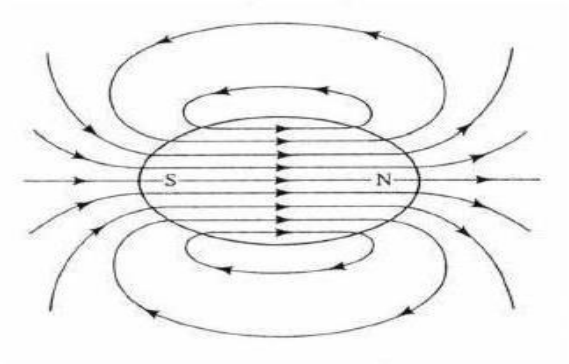

Figure 1.5. The **B** field of an ellipsoid magnet in zero applied field.

For a general ellipsoid, the expression for the magnetostatic energy is:

$$E_{ms} = \frac{1}{2}N_d M_a^2 + \frac{1}{2}N_b M_b^2 + \frac{1}{2}N_c M_c^2 \tag{1.29}$$

hence in the ab plane the magnetic shape anisotropy constant can be expressed as

$$K_s = \frac{1}{2}(N_b - N_a)M^2 \tag{1.30}$$

In general, the demagnetizing field along the short axis is stronger than that along the long axis; therefore, it is necessary to apply a higher magnetic field along the short axis in order to orient the magnetization in this direction as is shown in Figure 1.5.

The role of shape anisotropy is of great importance in our work where we investigate polycrystalline films of Permalloy. The samples which are used in our research are not ellipsoids; therefore, H_d is not uniform and in order to explore the effect of the non-uniformity on the magnetic configuration we have used numerical methods.

1.5 Magnetization Reversal.

1.5.1 Nucleation.

When an external magnetic field is applied on a sample with an antiparallel magnetization direction, it is energetically favorable for the magnetization to flip its orientation. Since an energy barrier is associated for this flipping, it occurs by nucleating a small region which reverses its magnetization. The act of nucleation is followed by expansion/propagation and/or more nucleations in other areas until full reversal is achieved. The size of the nucleation area is determined by factors such as the energy gained by the magnetostatic energy and the energy loss due to exchange interaction, that is proportional to the nucleation area.

The problem of magnetic nucleation in the case of magnetization reversal was addressed by Gunther and Chudnovsky [29, 30]. They considered two states of energy minimums: local minima for the case where the magnetization

is oriented to the +z direction and absolute minima for magnetization pointing to the -z direction. The appearance of nucleation is followed by propagation until all sample space is magnetized into a single direction.

1.5.2 Single Domain Reversal.

A single-domain particle is one in which the single-domain state possesses the lowest energy states. The size range for which a ferromagnet becomes single-domain is generally quite narrow. For most magnets, it is in the order of 10-100 nm. The size range is narrowed between two configurations; the lower limit corresponds to the transition to superparamagnetic state where as the formation of multiple magnetic domains can be observed for the upper limit. When the magnetization process occurs in a single domain particle, applying an external magnetic field H at an angle α with respect to the EA will tilt the magnetization to an certain angle θ with respect to the EA (See Figure 1.6). The angle θ is determined by minimizing the Stoner Wohlfarth Hamiltonian (SW) [31-33]:

$$H = K_s \sin^2 \theta - M_s H \cos(\alpha - \theta) \qquad (1.31)$$

where the first term corresponds to the uniaxial anisotropy (crystalline or shape) and the second is due to the interaction between the external field **H** and the saturated magnetization M_s.

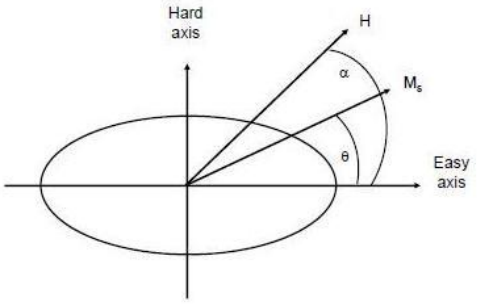

Figure 1.6: An illustration of a single magnetic domain with an elliptical shape under an external magnetic field (H) applied at an angle α with respect to the EA. The magnetization in this case is rotated by an angle θ from the EA.

From this Hamiltonian, we can find the equilibrium position of the magnetization by finding the extremal points.

$$\frac{dH}{d\theta} = 2K_s \sin\theta\cos\theta - M_s H \sin(\alpha - \theta) = 0 \tag{1.32}$$

or

$$\sin\theta\cos\theta = \frac{H}{H_k}\sin(\alpha - \theta) \tag{1.33}$$

where

$$H_k = \frac{2K_s}{M_s} \tag{1.34}$$

is known as the anisotropy field.

Based on the model above, the minimum magnetic field that is needed to switch the magnetization, $h_{SW} = \frac{H_s}{H_k}$ (where H_s is switching field), depends on the direction of the applied magnetic field (See Figure 1.7). For example, if the applied magnetic field is at an angle of $\alpha = 90°$ or $\alpha = 180°$, the

switching field exhibits a maximum at $h_{SW} = 1$. Conversely, if the applied magnetic field is at an angle of $135°$, the switching field has a minimum at $h_{SW} = 0.5$

Generally $h_{SW} = \frac{H_S}{H_k} = \frac{1}{[\sin^{2/3}(\theta)+\cos^{2/3}(\theta)]^{3/2}}$.

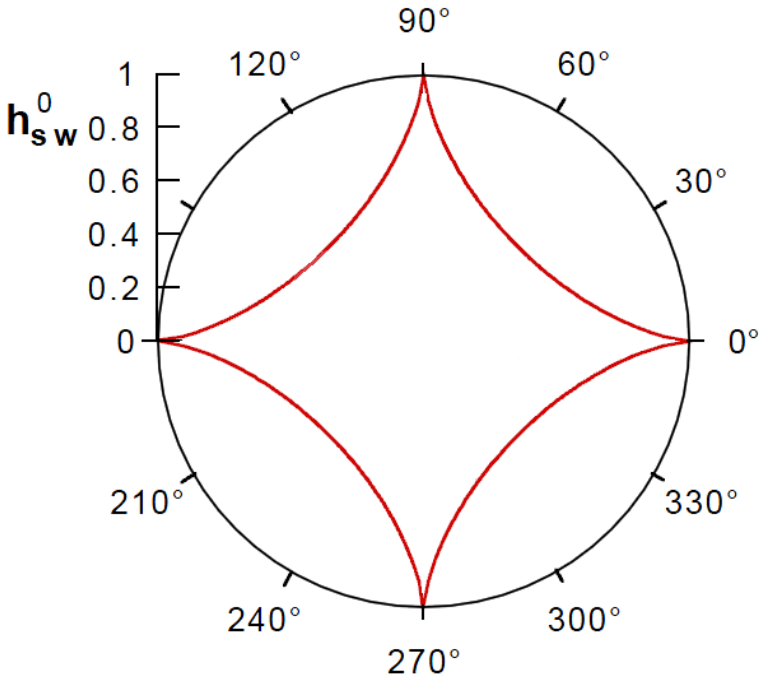

Figure 1.7: The switching field, h_{SW} , as a function of α. Inside the astroid domain is made of the field values for which a reversal of the magnetization is possible. Outside the astroid domain, no reversal is possible.

For more details please refer to our first article where we show that shape anisotropy induces effective single domain behavior in elliptical structures of thin permalloy films with long axis ranging between several microns to several millimeters.

In our research, we use the SW model to develop and characterize the PHE sensor that behaves like a single magnetic domain. The single magnetic domain behavior keeps the sensor gain stable and reproducible over time and also considerably reduces its 1/ f noise [34].

2. Materials.

2.1 Introduction.

This chapter provides background information on NiFe Alloys, their physical properties and applications. In addition to the general information, this chapter provides a detailed description of the thin films prepared for elliptical PHE sensors.

2.2 NiFe Alloys.

Generally, magnetic materials for industrial purposes are divided into two categories:

a) hard magnetic materials - materials that have high coercive fields and
b) soft magnetic materials which are easier to magnetize and have high permeability.

Between 1913 to 1921, Gustave Elman and his associates developed a new alloy containing nickel and iron elements with different relations (more information on the history of their investigation can be found in the book of Bozorth [35]. These alloys are commonly known as Permalloy (Py). In most cases the name is followed by a number representing the percent of nickel in this alloy.

In our work we used Py with 80 percent nickel. Py 80 has $T_c = 853$ K and a very high permeability. The permeability value depends on the sample treatment and subsequent processing; in some cases, initial permeability of 8000 and a maximum permeability of 100000 can be observed. The

coercive field [36] of Py 80 is 0.5 Oe or less [37] and the magnetization saturation (M_S) is ~800-1100 Oersteds.

Depending on crystallinity, heat treatment and different growth methods, the room temperature resistivities of Py 79, 80, 81 in the order of $20-40\,\mu\Omega$cm can be achieved. Additionally, this is significantly influenced by the applied magnetic field [38] and the AMR of Permalloy films can vary between 1.5 to 5% [3-7, 26]. In permalloy 80, the scattering of spin down electrons can be 5 to 10 times higher than spin up electrons which implies mean free path $\frac{\lambda_\uparrow}{\lambda_\downarrow} = 5$ to 10 (typically $\lambda_\uparrow = 6$ nm and $\lambda_\downarrow = 1$ nm 28 at 300 K) [39].

Permalloy has an important role in a variety of electrical components like loading coils, transformers, magnetic amplifiers, relays, flux gates and AMR sensors (for different applications including recording, read head sensors and so on.). The presence of (111)-preferred crystallographic orientation in polycrystalline Permalloy films usually makes the film magnetically softer hence makes it better for sensing applications [40].

The magnetic properties of soft magnetic material are not necessarily determined by the magnitudes of anisotropy but also by distortions in the crystalline structure. In general, the presence of grain boundaries, non-magnetic insertions and internal stresses [41] leads to the modification of the magnetic properties in these materials.

There are several ways to deposit Permalloy films, including magnetron sputtering, ion beam deposition, thermal

evaporation and so on. In our work, we have used magnetron sputtering as a method to prepare our Permalloy thin films.

3. **Magnetoresistive Sensors.**

3.1 Introduction.

This chapter provides background information on magnetoresistive sensors

The chapter is divided into three sections:

1. The first section describes the general concept of AMR sensors.
2. The second section deals with the PHE sensors and their types.
3. The third section gives an overview of Elliptical PHE Sensors. In addition, we will describe in detail about the elliptical sensors fabricated in our group which is one of its kind.

3.2 AMR Sensors

Anisotropic Magnetoresistive (AMR) sensors can take different shapes and forms [13, 42-48] during fabrication. Typical AMR sensors can sense external DC and AC magnetic fields as well as the strength and direction of the field. These sensors are made of a nickel-iron (Permalloy) thin film deposited on a silicon wafer and patterned as a resistive strip on which metal stripes (so-called barber poles, see Figure 3.1-3.2a) are deposited. This leads to the linear sensing behavior with the externally applied field (a small change in the magnetization orientation gives proportional change in the

resistance) [13]. The spontaneous magnetization lies along the *easy axis* direction which is determined by the shape anisotropy. It has to be noted that for the fabrication of the AMR sensor, one need to define the easy axes in the system externally. This can be achieved by exploiting different kinds of anisotropy for instance shape, field or exchange induced anisotropy. A magnetic field along the *hard axis* (perpendicularly to the EA) causes a rotation of the magnetization in the Permalloy strip leading towards the change in its resistance.

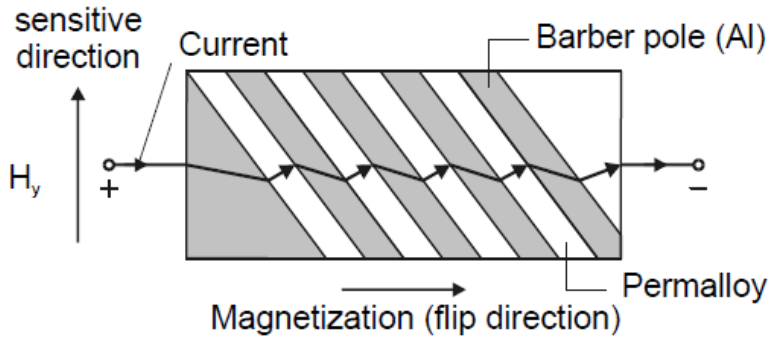

Figure 3.1: Barber poles on permalloy stripe.

Figure 3.2b depicts the AMR sensors implemented in a four-element form known as a Wheatstone bridge. Though theses bridge sensors provides diverse features suitable for the device implementation, the presence of the anomalous output voltage known as an "offset" voltage without applying any magnetic field, hinders its performance. In this regard, it is important to compensate the "offset" voltage with some external means.

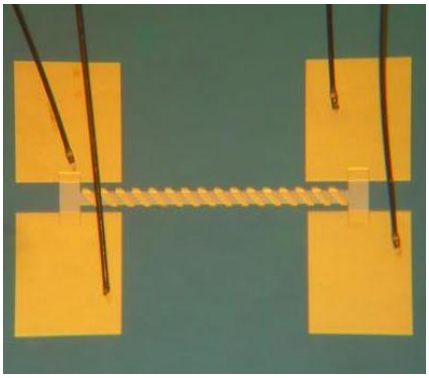

b)

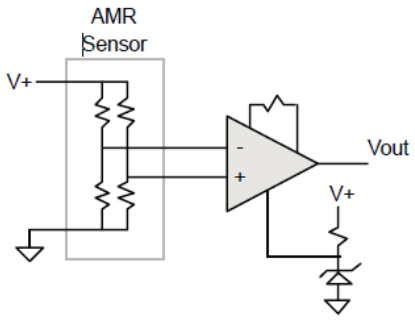

Figure 3.2: An AMR sensor (a) and a Wheatstone bridge circuit (b).

The best known commercial AMR sensors[49] have a noise of ~100 $^{pT}/_{\sqrt{Hz}}$ at 1 Hz, however it is difficult to achieve pT noise values with the whole AMR magnetometer [50]. Comparative measurements of minimum detectable signal for different MR sensors are shown in Figure 3.3.

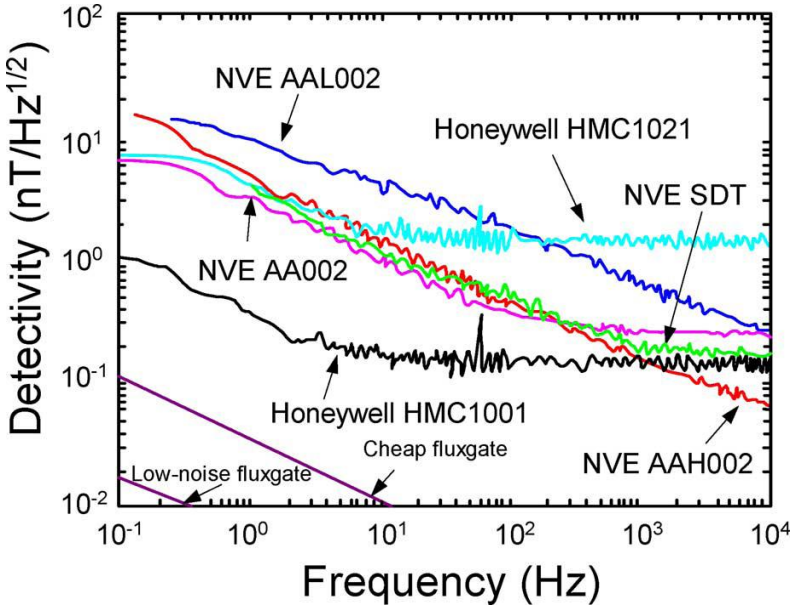

Figure 3.3 Noise spectrum of AMR, GMR and fluxgate sensors [27]. HMC 1001 and 1021 are AMR magnetoresistors, NVE AAxx are GMR magnetoresistors, and NVE SDT is a prototype of a spin-dependent tunelling device. The data for a "cheap fluxgate" represent typical noise of Applied Physics Model 533 and similar devices. The data for "low-noise fluxgate" is taken from [28]. Adopted from [29].

3.3 PHE Sensors

In the PHE sensor, the output signal depends on the angle between the magnetization direction in the magnetic conductor and the direction of the current flow through it. This characteristic is used for the detection of the feeble magnetic field [48, 51, 52]. For such a use, the magnetic conductor should have uniform magnetization, and the magnetization direction should change following the theoretical model of magnetization reversal proposed by Stoner Wohlfarth. In addition, the magnetization change should be reversible and it should not exhibit any hysteresis with the applied field. To obtain such a behavior, the layer should have magnetic anisotropy, commonly with an easy axis parallel to the current direction. When these conditions are met, the PHE signal indicates the magnetization direction thus indicating the magnitude of the applied magnetic field in the film plane which is perpendicular to the current direction as well.

In comparison to the AMR sensors, PHE sensors have several intrinsic advantages. The AMR as a function of the angle θ between the current and the magnetization has its largest slope at $\frac{\pi}{4} + n\pi$ whereas the PHE as a function of θ has its largest slope at $n\pi$. Since it is easier to fabricate sensors where in the absence of an applied magnetic field, θ is equal to $n\pi$ PHE sensors are simpler and cheaper to manufacture.

Furthermore, the AMR signal is measured on top of a large DC component associated with the average resistance (see Figure 1.2a). Therefore, temperature and aging drifts which affect the DC component are extremely detrimental to AMR sensors. To obtain an output voltage which reflects the AMR

signal without any DC component, AMR sensors are commonly used in a Wheatstone bridge configuration. Such a design is not needed in PHE sensors whose DC component is zero (see Figure 1.2b).

Different types of PHE sensors have been reported:

(a) Sensors with a single ferromagnetic layer with magnetic anisotropy which is induced during growth by applying a magnetic field and by using an antiferromagnetic pinning layer.

(b) Sensors with multi ferromagnetic layers separated by non-magnetic conductors. These sensors are commonly called spin valve PHE sensors.

(c) Sensors known as PHE Bridge (PHEB) sensors which employs common Wheatstone bridge configuration. It has to be noted that, these sensors are in reality the AMR not PHE sensors

(d) Sensors with a single ferromagnetic layer and shape induced magnetic anisotropy due to their elliptical shape. In this type of sensors, the best reported magnetic field resolution can be achieved and we will elaborate the properties of these sensors in the following sections.

a. PHE sensors with field induced magnetic anisotropy:

Uniform and reversible response of the ferromagnetic layer in a PHE sensor has been obtained by inducing uniaxial magnetic anisotropy during growth. A common structure of such sensors consists of a ferromagnetic $Ni_{80}Fe_{20}$ layer coupled to an antiferromagnetic IrMn layer. A field in the order of several hundreds of Oersteds induces magnetic anisotropy and aligns the pinning direction of the IrMn layer [53-56]

b. Spin-valve PHE sensors.

PHE sensors consisting of at least two ferromagnetic layers separated by non-magnetic layers are commonly called PHE sensors with spin-valve structure. This term refers to the fact that such magnetic multilayer structures are used to obtain a spin-valve effect; namely, that for a given voltage the current flow is high or low depending on the relative orientation of the magnetization in neighboring magnetic layers (parallel or anti-parallel). In the following section, the spin valve structures which are being used to fabricate PHE sensors are described in detail.

A common structure used for spin-valve PHE sensors is Ta/$Ni_{80}Fe_{20}$/Cu/$Ni_{80}Fe_{20}$/IrMn/Ta [57-72]. The structure is commonly deposited on silicon dioxide using DC magnetron sputtering system. The first Ta layer is a seed layer, the first $Ni_{80}Fe_{20}$ layer is the free magnetic layer, the Cu layer serves as the non-magnetic metallic spacer, the second $Ni_{80}Fe_{20}$ layer is the pinned ferromagnetic layer, the IrMn layer is an antiferromagnetic layers that pins the $Ni_{80}Fe_{20}$ layer below, and the second Ta layer is a capping layer.

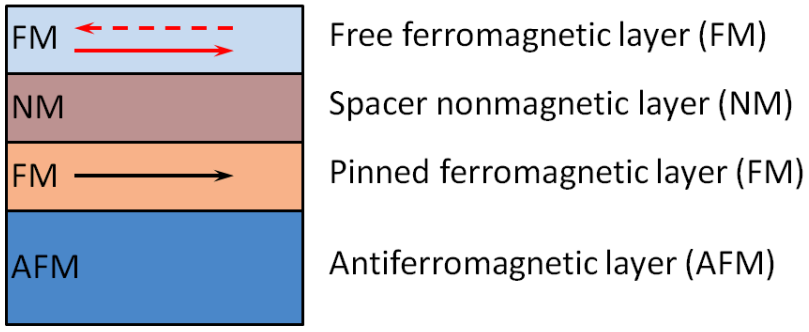

Figure 3.4: A typical layer structure of a spin-valve PHE sensor.

The layers are commonly sputtered in a working pressure of several mTorr with a magnetic field on the order of several

hundreds Oersted parallel to the film plane. The role of the field is to induce magnetic anisotropy in the ferromagnetic layers and define the exchange bias between the antiferromagnetic layer and the neighboring ferromagnetic layer. Typical thicknesses are: Ta – 5 nm, free NiFe – 4-20 nm, Cu – 1-4 nm, pinned NiFe - 1-12 nm, IrMn – 10-20 nm.

A sensitivity of 15.6 mΩ/Oe was reported for a structure with free layer thickness of 20 nm and pinned layer thickness of 2 nm [73]. Other reports indicate sensitivity of less than 10 mΩ/Oe [60, 65, 68, 74]. Other spin valve structures include Co/Cu/Py [75-77], Co/Cu multilayers [78], NiFe/FeMn/NiFe [79], and Ta/NiFe/CoFe/Cu/CoFe/IrMn/Ta [58]. However, for these structures either sensitivity data are missing or the sensitivity is lower than for the $Ta/Ni_{80}Fe_{20}$/Cu/Ni80Fe20/IrMn/Ta structures.

In these sensors the spin valve structure is used to induce the required magnetic properties. There are no reports of additional transverse voltage in relation to the spin valve effect itself; namely, the large variations in the longitudinal resistivity as a function of the magnetic configuration. The measured PHE signal is simply the average contribution of all layers in connection with the AMR of each layer.

c. PHE Bridge sensors:

The term PHE bridge (PHEB) sensors [53-56, 68, 80-84] has been used to describe AMR sensors in different Wheatstone bridge configurations. Two main types have been considered: (a) sensors where the arms are straight and form a square; (b) sensors where the arms form a ring shape [84]. The two basic

shapes have been further developed into meander-like shapes to increase the signal (see Figure 3.5). In all these configurations at zero applied field the angle between the internal magnetization and the current is around 45 degrees as required for AMR sensors and not parallel or anti-parallel as required for PHE sensors.

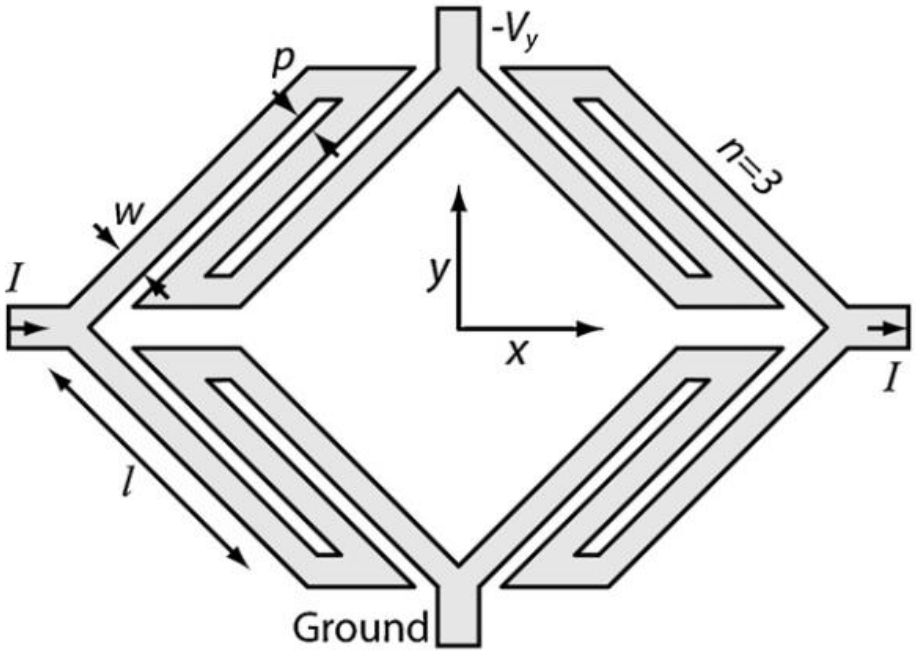

Figure 3.5: Planar Hall effect Bridge (PHEB) configuration with multi segments per branch (Source: Reference [54] The bridge configuration which is useful for eliminating effects of thermal drifts, and the angle between the current and the internal magnetization when no field is applied give rise to a dependence of the output voltage on the magnetization direction which is similar to that obtained for PHE; nevertheless, these are in fact AMR sensors whose output is determined by the integrated AMR response of the entire bridge structure. Such sensors have demonstrated a resolution of 2 nT/√Hz at 1 Hz [54].

3.4 Elliptical PHE Sensors.

We fabricated and explored Elliptical PHE sensors. The elliptical shape of these sensors induces uniaxial magnetic anisotropy parallel to the long axis of the ellipse. For sensing, a current is driven along the long axis of the ellipse and the transverse voltage due to the PHE is measured across the short axis of the magnetic ellipse (See Figure 3.6).

It has to be noted that, since the uniaxial magnetic anisotropy can be tuned externally, the field range in which these sensors are operating can be tuned as well. This motivates us to investigate these systems further. The details of the fabrication procedure, its working principal and corresponding analytical model will be described in the following section.

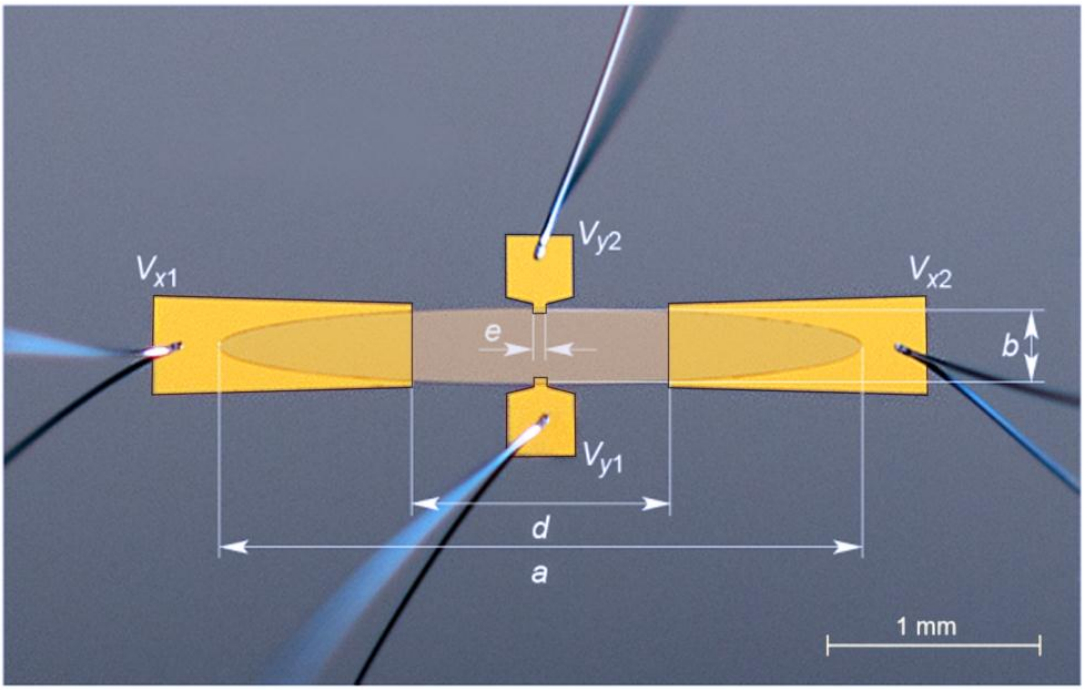

Figure 3.6: An elliptical PHE sensor with its dimensions. The elliptical part is made of Permalloy capped with tantalum. The current leads (V_{x1},V_{x2}) and the voltage leads (V_{y1},V_{y2}) are made of gold.

4. Experimental Details.

4.1 Introduction.

This chapter is divided into four sections:

1. The first section describes the sample fabrication process and gives overview of the elliptical structures that were designed for this study.
2. The photo and e-beam lithography processes used for the final structure fabrication are described in the second section.
3. The final section deals with the measurement methods. Initially, we describe the homemade system which was designed and built for the transport measurement at room temperature. Afterwards, we describe sensor noise measurement technique that has been exploited to find the equivalent magnetic noise of our elliptical sensors.

In addition, we discuss the external electronics needed for the measurements as well as different measurement configurations.

4.2 Sample Fabrication.

The elliptical PHE sensors are fabricated by the following steps:

Starting with undoped Si wafer (orientation: (100) ± 0.9°, resistivity > 100 Ω cm, micro roughness ≤ 5A°.

1. Ellipses are patterned on the wafer by a liftoff process using MJB-4 Mask aligner (Figure 3.7), photoresist S1813 and developer MICROPOSIT® MF®-319.
2. Permalloy ($Ni_{80}Fe_{20}$) films capped with tantalum are sputtered in a UHV-evaporation and sputtering system (BESTEC). Prior to deposition, the wafer is treated with Ar^+ beam using 3cm DC Ion Source Filament Cathode

(ITI) in order to remove resist and developer residue that can remain after development process. Base vacuum before deposition is less than $5 \cdot 10^{-7}$ mBar, and it rises to $3 \cdot 10^{-3}$ mBar during deposition. Gas is introduced into the upstream end of the ion source through the gas feed tube where it is ionized. The Permalloy is sputtered at a rate of 1.76 $^{A^{\circ}}/_{S}$ and a capping layer of tantalum (3 nm) is deposited on top in situ immediately after Permalloy to prevent oxidation.

The coercive field of the films was ~2 Oe and M_s about 820 emu/cm³.

3. Following these, the wafer is immersed in acetone or NMP for liftoff.
4. Current and voltage leads are patterned using second liftoff process.
5. The gold contacts are sputtered on top of an adhesion layer of chrome (4 nm) in BESTEC. Before deposition the wafer is treated with Ar^+ beam. The gold layer thickness is ~1.5 times the thickness of the magnetic layer.
6. The wafer is immersed in acetone or heated NMP for liftoff.

The liftoff process described in (2), (3) and (4) can be replaced by a wet etching process. In this process, the step (3) should be carried out after step (1) and the next step involves a reversed lithography (namely the remaining photoresist defines

the ellipses. Stage (4) is replaced by wet etching with 32% HCl. The etching is stopped by H_2O.

4.3 Patterning.

For some of our patterns photolithography process using a Mask Aligner was useful. To fabricate samples with an approximate resolution of microns we used the SUSS MJB4 Manual Mask Aligner. This machine has the ability to fabricate features with a resolution of 0.5 μm over standard 4 inch silicon wafer.

The photo lithography process consists of several steps. The first step is to coat the sample with a photo-resist that is sensitive to ultraviolent light, and to bake it for a few minutes. The second step is to expose the resist to ultraviolent light through a shadow mask made of chromium, and then immerse the sample in a development solution to remove the exposed resist. The final step is to etch the sample or deposit materials for lift off, and then remove the resist polymer with acetone to reproduce the mask pattern on silicon wafer. Sometimes the lithography process might be more complicated. For example, in order to create golden leads connecting magnetic sensors to main circuit one needs to use two or more masks using special marks to obtain best alignment.

Figure 4.1: SUSS MJB4 Manual Mask Aligner

The e-beam lithography process is quite similar to the photo lithography process. In this process, instead of ultraviolet light we use electrons to draw our pattern on the resist coated sample, as opposed to the mask used for the photo-lithography. This pattern is created using AUTOCAD or CABLE software. The rest of the process is similar to the process described for photo-lithography. Using the e-beam lithography one can obtain structures with submicron and even nanometer dimensions. We used nanolithography to characterize magnetic film. We have also used e-beam in order to prepare Py ellipses with different sizes and aspect ratios.

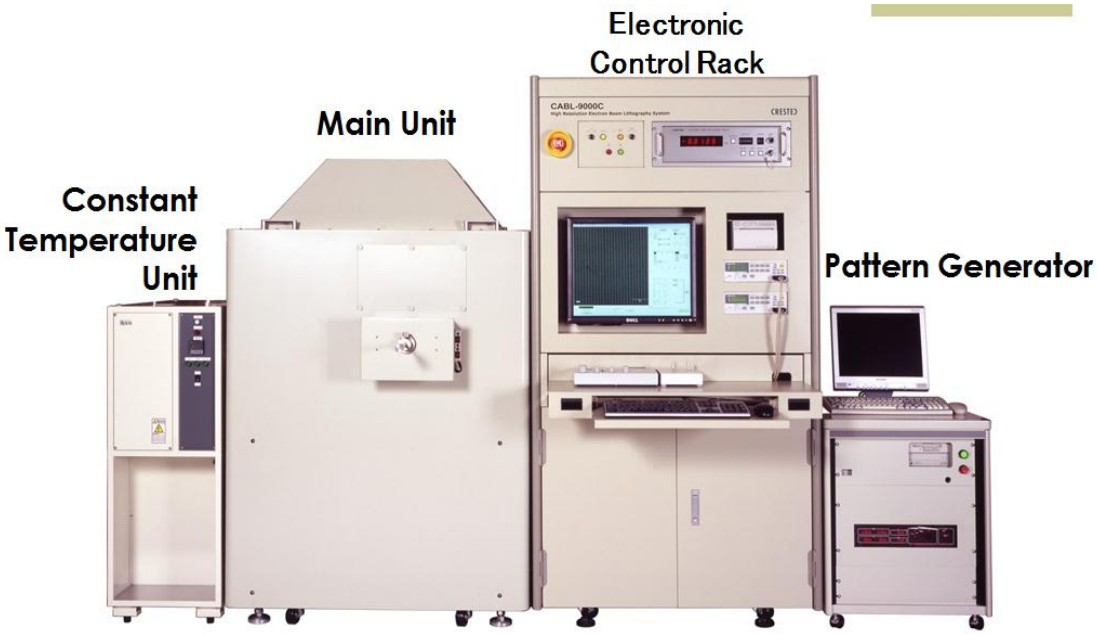

Figure 4.2: CRESTEC, CABL-9500C e-Beam Lithography system.

4.4 Measurement Systems.

4.4.1 Response measurements (DC).

For DC measurements we have developed a home-made system in the lab. The system is composed of two pseudo Helmholtz coils built of aluminum structure and windings were done by the isolated copper wire. The copper length for each coil is of 2500 meters. The interior radius is 38 mm and the exterior is 44.5 mm. The coils were designed to give a field change $^{\Delta B}/_{B}$ of 3×10^{-7} Oe to a point located 5 mm aside (with the same distance from the two coils) for an external magnetic field of 372.6 Oe (compatible to a current of 1.8 A) field value sample laying between the coils. The sample itself is set on a stage that can rotate using a brushless motor (Faulhaber DC 24SR Micromotor) that is connected to a gear system. The stage can rotate more than 360° with an angle

resolution of 0.03°. The sample is connected electrically to a switch box (Keithley 7001), a current source (Keithley 2400), and a nanovoltmeter (Keithley 2182). All measuring devices are computer controlled. The system itself is confined inside a metallic cage in order to reduce noise.

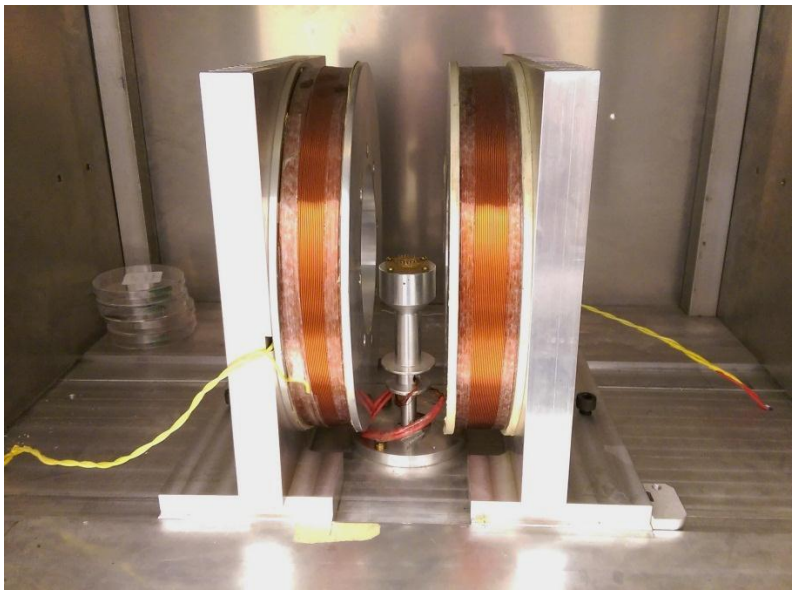

Figure 4.3: pseudo Helmholtz coils system.

4.4.2 Noise measurements (AC).

The equivalent electrical circuit of the PHE sensor and its preamplifier is presented in Figure 4.4. The equivalent circuit includes the PHE voltage source which generates a V_y voltage across the sensor y-terminals. Here, R_y, $e_{external}$,$e_{1/f}$ and e_{amp} denotes the sensor resistance across the y-terminals, external noise due to thermal fluctuations and structure imperfections, $1/f$ noise and the total preamplifier noise respectively. In addition, the voltage noise, current noise, and the noise of the feedback resistors R_f, and R are also depicted in the following figure 4.4.

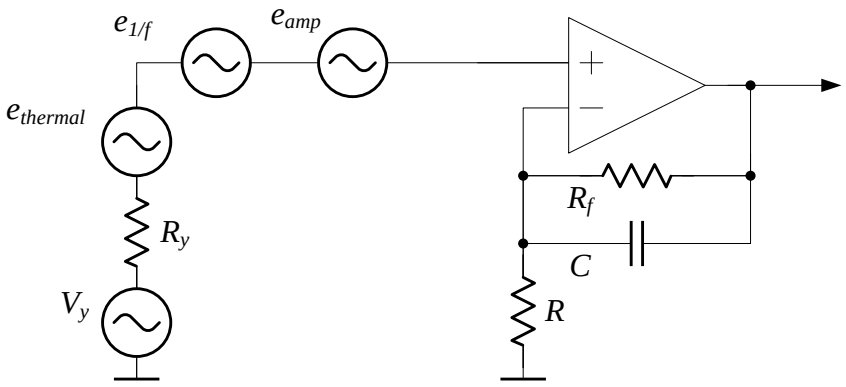

Figure 4.4: Equivalent electrical circuit of the PHE sensor.

a. Signal

The sensitivity of a PHE sensor is defined as the ratio between the PHE voltage V_y and the magnetic field B applied in the film plane perpendicular to the easy axis (and the current direction). When B is small compared to the total effective anisotropy field (H_k) which is the sum of the sensor shape induced anisotropy H_{sa} and the excess anisotropy H_{ea} , the sensitivity can be expressed as follows [11]:

$$S_y = \frac{V_y}{B} = 10^4 \frac{V_x}{R_x} \cdot \frac{\Delta\rho}{t} \cdot \frac{1}{H_{sa} + H_{ea}} \qquad (4.1)$$

where V_x is the bias voltage across the x-terminals, R_x is the sensor resistance across the x-terminals, t is the sensor thickness, and $\Delta\rho$ is the sensor average electrical resistivity ($\Delta\rho = \rho_{\parallel} - \rho_{\perp}$).

We express the sensor resistance across the x-terminals R_x, while neglecting the resistance of the gold leads and the interface resistance between the leads and the sensor as:

$$R_x = \frac{C_1 \cdot \rho \cdot d}{t \cdot b} \tag{4.2}$$

In this expression, C_1 is a constant not much larger than 1 which is used to reflect the previously mentioned approximations.

b. Noise

The total noise of a PHE sensor e_Σ has three main components: $1/f$ noise, thermal noise, and preamplifier noise:

$$e_\Sigma = \sqrt{e_{1/f}^2 + e_{\text{thermal}}^2 + e_{amp}^2} \tag{4.3}$$

Thermal noise

The thermal noise (sometimes referred to as Johnson noise) is generated by thermal agitation of electrons in a conductor and is defined by:

$$e_{\text{thermal}} = \sqrt{4k_B T R_y} \tag{4.4}$$

where k_B is the Boltzmann constant, T is the temperature, and R_y is the sensor resistance across the y-terminals:

$$R_y = \frac{C_3 \cdot \rho \cdot b}{t \cdot e \cdot C_2} \tag{4.5}$$

where C_3 is a constant not much larger than 1, and C_2 is a constant larger than 1 relating the real, rectangle shaped

volume between the *y*-terminals to the effective conduction area.

1/f noise

The sensor $1/f$ noise is described using the Hooge empirical formula:

$$e_{1/f} = \sqrt{V_x^2 \frac{\delta_H}{N_c \cdot Vol \cdot f^{\alpha}}} \tag{4.6}$$

where V_x is the bias voltage, δ_H is the Hooge constant [34, 85], N_c is the "free" electron density and is equal to 1.7×10^{29} for $Ni_{80}Fe_{20}$ Permalloy [85], f is the frequency, α is a constant, and *Vol* is the effective volume, where the electrons are contributing to the conduction process in a homogeneous sample [85].

Considering the effective conduction volume described in Equation 4.5, *Vol* can be approximated by:

$$Vol = C_2 \cdot t \cdot \rho \cdot d \tag{4.7}$$

Amplifier noise

e_{amp} is the total preamplifier noise (including the voltage noise, current noise, and the noise of the resistors). The feedback resistors R_f and R are selected to be small enough so that their noise contribution can be neglected. Consequently,

$$e_{amp} = \sqrt{v_{amp}^2 + \left(R_y i_{amp}\right)^2} \tag{4.8}$$

where v_{amp} and i_{amp} are the operational amplifier voltage and current noise respectively. The voltage and current noise of the operational amplifier possess both white and pink ($1/f$) noise components and can be expressed using the following expressions:

$$v_{amp} = v_{amp0}\sqrt{1 + \frac{f_{c1}}{f^{\alpha_1}}} \tag{4.9}$$

$$i_{amp} = i_{amp0}\sqrt{1 + \frac{f_{c2}}{f^{\alpha_2}}} \tag{4.10}$$

where v_{amp0} and i_{amp0} are the level of the voltage and current white noise densities respectively, f_{c1} and f_{c2} are the voltage and current noise densities corner frequency respectively and α_1 and α_2 are constants.

c. Equivalent magnetic noise

The sensor equivalent magnetic noise (sometimes referred to as resolution or minimal detectable field) is defined as

$$B_{eq} = \frac{e_\Sigma}{S_y} = \frac{\sqrt{e_{1/f}^2 + e_{\text{thermal}}^2 + e_{amp}^2}}{10^4 \frac{V_x}{R_x} \cdot \frac{\Delta\rho}{t} \cdot \frac{1}{H_{sa} + H_{ea}}} \tag{4.11}$$

In the following sections, we describe a series of steps we have made to improve the magnetometer resolution with special

emphasis on the low frequency noise.

4.4.3 Operation and optimization of elliptical PHE sensors

Exciting the sensor using ac current as previously explained, the preamplifier consists of voltage and current noise sources at its input, both possessing white and $1/f$ components (see Equations 4.9 and 4.10). Our magnetometer is designed for optimal resolution at ultra-low frequencies starting from the mHz range. Since the $1/f$ noise of the elliptical PHE magnetometer is extremely low, even ultra-low noise operational amplifiers will introduce an additional, significant $1/f$ noise at frequencies below 1 Hz (see for example LT1028 by Linear Technology). A probable solution is to use chopper or auto-zero amplifiers. Those amplifiers show minimal drift and zero $1/f$ noise at their input. However, even state-of-the-art commercially available amplifiers of this type (see for example ADA4528-1 by Analog Devices) demonstrate white noise levels five times higher compared to the white noise level of a standard ultra-low noise operational amplifier and therefore did not constitute a potential solution in this case.

To overcome this limitation we have excited our sensor using ac current as opposed to the classic approach of dc current excitation. Exciting the sensor using ac current translates its output signal and its intrinsic thermal and $1/f$ noise to frequencies where the $1/f$ noise of the preamplifier can be neglected. The preamplifier output signal can then be demodulated back to baseband using analog or digital synchronous detector.

Compared to chopper amplifiers which modulate the signal inside the amplifier, modulation of the signal inside the sensor itself results in an equivalent white noise behavior of the amplifier with a drastically lower noise level.

Figure 4.4 shows the amplitude spectral density of the LT1028 preamplifier equivalent input noise, measured after demodulation without excitation current. One can see that the preamplifier noise is white from 10 mHz to 100 Hz. The measured white noise level of $\sim 1.1\,\mathrm{nV}/\sqrt{\mathrm{Hz}}$ is in good agreement to the reported white noise level in the LT1028 op-amp datasheet. The graph in Figure 4.4 was acquired using a digital demodulation at a frequency of 1.12 kHz.

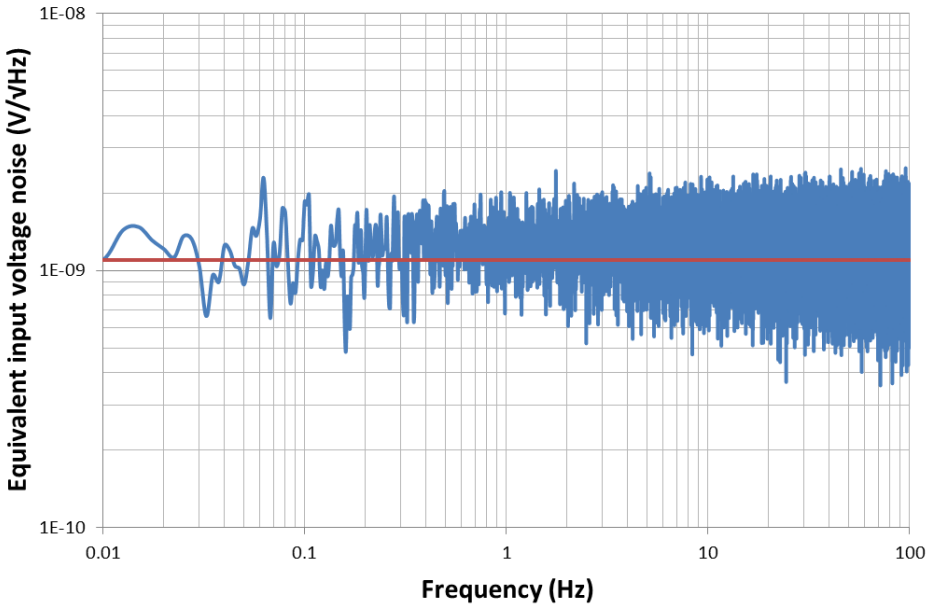

Figure 4.4: Equivalent input voltage noise versus frequency for a LT1028 operational amplifier with an output demodulation at 1.12 kHz. Both the measured noise and the fit are shown (blue and red line respectively).

Optimization of the sensor thickness

The PHE sensor $1/f$ noise is inversely proportional to the sensor volume (see Equation 4.6). Since the sensor signal is inversely proportional to the sensor thickness, it is also inversely proportional to its volume (see Equation 4.1). As a

result, there is an optimal thickness for which the sensor equivalent magnetic noise is minimal.

Our magnetometer is optimized to operate at ultra-low frequencies where the $1/f$ noise component of the sensor is dominant over its thermal noise and the preamplifier white noise. In the limit where the $1/f$ noise is dominant, only the first term under the square root of Equation 4.3 remains relevant. The parameters H_{ea}, $\Delta\rho/\rho$, and ρ do not depend on the sensor thickness for t > 20 nm; therefore, they are considered as constants for the thicknesses we use. By substituting the expressions for H_{sa}, R_x, Vol and R_y, into Equation 4.11 we obtain:

$$B_{eq} = \sqrt{\frac{\delta_H}{N_c \cdot C_2 \cdot t \cdot b \cdot e \cdot f^{\alpha}}} \frac{(10^4 t + b + H_{ea}) \cdot C_1 \cdot d \cdot \rho}{10^4 \cdot \Delta\rho \cdot b^2} \qquad (4.12)$$

We note that the equivalent magnetic noise in Equation 4.12 depends only on the sensor dimensions and the material properties. Optimizing *t* for minimal value of B_{eq} yields:

$$t_{opt} = \frac{H_{sa} \cdot b}{10^4} \qquad (4.13)$$

We find that for this thickness:

$$H_{sa} \approx H_{ea} \qquad (4.14)$$

To appreciate the sensitivity of B_{eq} on deviations from the optimal thickness, we calculate changes in B_{min} denoted as

$B_{eq} = B_{min} \cdot \delta B_{eq}$ as a result of relative changes in the sensor thickness denoted as $\delta t = (t_{opt} \pm t)/t_{opt}$. This yields

$$\delta B_{eq} = \frac{1}{2}(1 + \delta t)\sqrt{\frac{1}{\delta t}} \tag{4.15}$$

A plot of Equation 4.15 (Figure 4.4) shows that a ten-fold deviation of the sensor thickness from its optimum value results in almost two-fold increase in the sensor equivalent magnetic noise.

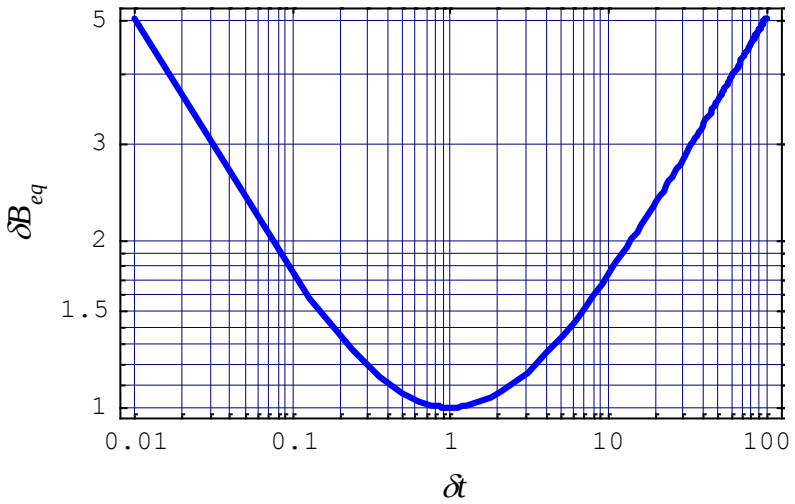

Figure 4.4: Relative change in the equivalent noise as a result of deviations from the optimal thickness.

We now substitute Equation 4.15 into Equation 4.16 and obtain the sensor low-frequency equivalent magnetic noise at the optimal thickness:

$$B_{min} = \sqrt{\frac{\delta_H}{N_c \cdot C_2 \cdot e \cdot f^a}} \frac{2\sqrt{H_{ea}} C_1 \cdot d \cdot \rho}{10^2 \cdot \Delta\rho \cdot b^2} \tag{4.16}$$

Optimization of the driving current

Theoretically, if the sensor power consumption is not limited, the excitation current should be as high as possible to bring the equivalent magnetic noise to a minimum at all frequencies. However, the ability of the sensor to dissipate the excessive heat is limited and therefore, at a too high current, the sensor becomes thermally unstable, which degrades its equivalent magnetic noise.

The excitation current should be selected according to the bandwidth requirements of the specific application. In frequencies significantly higher or lower than 1 Hz, thermal or $1/f$ noise, respectively, will dominant over other noise sources regardless of the excitation current. On the other hand, in the unique case of a bandwidth ranging from sub-Hz frequencies and up to tens or hundreds of Hz requires a more sophisticated approach for the selection of the excitation current based on an experimental optimization process.

In this case of intermediate frequencies the optimal current must yield best possible magnetic field resolution at frequencies where the $1/f$ noise dominants but also at frequencies where the white noise sources are dominant.

To find the optimal excitation current for the intermediate frequency range, we have measured the sensor equivalent magnetic noise between 0.01-10 Hz for currents in the range of 10-100 mA. We have changed the current by small steps measuring at each step the sensor gain and noise. Figure 4.5 shows the sensor equivalent magnetic noise as a function of frequency for three cases: a too high, a too low and optimal excitation current.

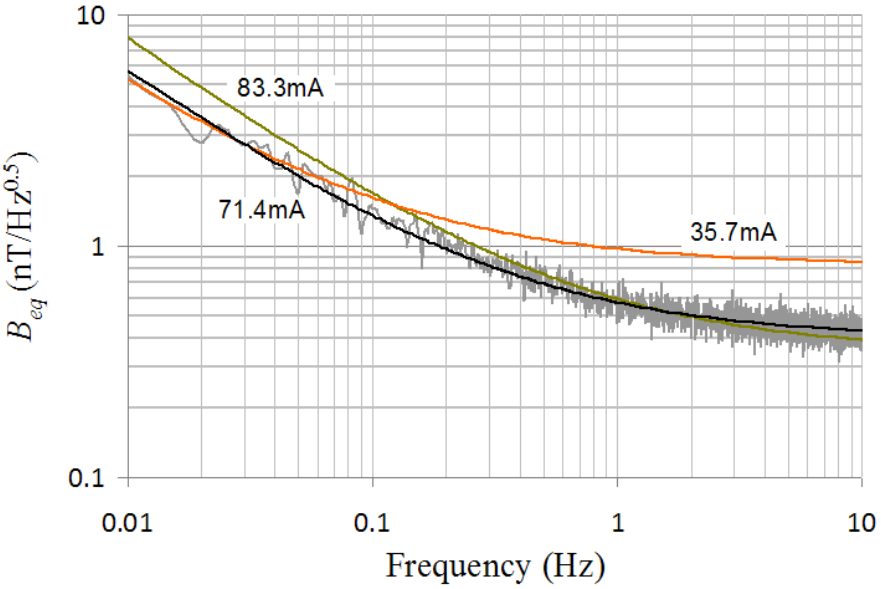

Figure 4.5: Equivalent magnetic noise versus frequency. For the optimum excitation current amplitude of 71.4 mA, both the sensor noise and the noise fit are shown. For other excitation current amplitudes only the noise fits are shown.

The sensor was excited with AC current. The sensor output was amplified using a low-noise operational amplifier (LT1028). The amplifier output was sampled by a 24-bit ADC (PXI-5421) and demodulated using a digital synchronous detector. A 100 Hz low-pass filter at the output of the synchronous detector was used to band-limit the signal. As the input voltage noise of the LT1028 operational amplifier flattens at around 1 kHz, we have excited the sensor at 1.22 kHz to avoid the amplifier $1/f$ noise and 50 Hz power network harmonics. The sensor gain was measured using a calibrated solenoid and was found to be flat from 10 mHz to 100 Hz. The sensor noise was measured by using a seven layer magnetic shield to suppress low-frequency interferences. A similar experimental setup is shown in Figure 4.6 The experimental sensor parameters are listed in Table. 1

Parameter	Value	Units	Parameter	Value	Units
a	3	mm	H_a	3.84	Oe
b	0.375	mm	H_k	3.45	Oe
t	120	nm	$\Delta\rho/\rho$	1.6	%
d	1.2	mm	ρ	$2.7\ 10^{-7}$	$\Omega\cdot$m
e	0.06	mm	α	1.5	
R_x	9.97	Ω	δ_H	$2.73\ 10^{-3}$	
R_y	5.08	Ω	N_c	$17\ 10^{28}$	$1/m^3$
I_x	71.4	mA			

Table 1. Parameters of the PHE sensor experimental model.

From Figure 4.5, one can see that the sensor equivalent magnetic noise at the optimal excitation current is either the lowest one or does not practically differ from the noise values at the other excitation currents. A too low excitation current provides similar results at low frequencies but worse results at higher frequencies, where the $1/f$ noise is not so dominant. At a too high excitation current, the equivalent magnetic noise at high frequencies is similar to that of the optimal current, but is degraded at low frequencies due to thermal drift.

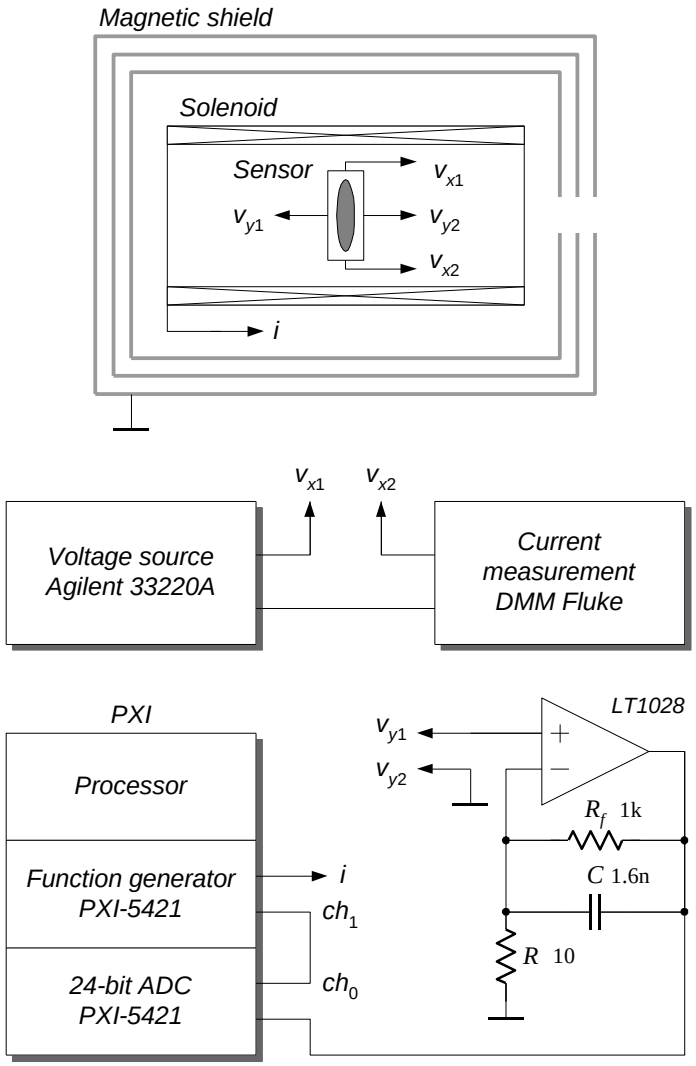

Figure 4.6: An experimental setup similar to the one used for the excitation current optimization process.

5. Numerical Simulations.

5.1 Introduction.

The final section gives an overview of The Landau Lifshitz Gilbert (LLG) Equation and numerical simulation program OOMMF.

5.2 The Landau Lifshitz Gilbert (LLG) Equation.

The equation of motion of the magnetic moment is commonly described by the Landau Lifshitz Gilbert (LLG) equation [86]

$$\dot{M} = -\gamma M \times H_{effective} + \frac{\alpha}{M_s}\left(M \times \dot{M}\right) \qquad (5.1)$$

where γ is the gyromagnetic ratio and α is a damping constant. The first term represents the precession of the magnetization around an effective field, and the second term represents damping towards the effective field axis. The effective field $H_{effective}$ is a combination of the external magnetic field H_{ext}, the demagnetizing field H_d, the anisotropy field H_a and the exchange interaction H_{ex}. In the case of uniformly-magnetized thin films, the demagnetizing field is $H_d = M_n$, where M_n is the component of the magnetization oriented normal to the film plane.

$$H_a = \frac{2K_u M_z \hat{z}}{\mu_0 {M_s}^2} \qquad (5.2)$$

where $\hat{z}$ is a unit vector along the easy axis. The exchange field is

$$H_{ex} = \frac{2A\nabla^2 M}{(\mu_0 M_s){M_s}^2} \quad (5.3)$$

where A is the exchange stiffness constant. Therefore the effective field can be written as:

$$H_{effective} = \left(\frac{2A\nabla^2 M}{(\mu_0 M_s){M_s}^2} + \frac{2K_u M_z \hat{z}}{\mu_0 {M_s}^2} - M_n + H_{ext}\right) \quad (5.4)$$

5.3 OOMMF Simulations.

OOMMF is an open source program that calculates the magnetization time evaluation by solving the LLG equation [87]. We used this program in our first publication [11] to understand different aspects of the magnetization reversal process such as the switching field and the reversal mode. Although this program does not account for temperature or quantum effects during calculation, it gives the good estimation for magnetic behavior of the permalloy-made ellipses.

6. Future prospects and applications.

The current sensitivity of the elliptical PHE-sensors exceeds the sensitivity of the most sensitive commercial AMR sensors and the sensitivity of other MR sensors. However, there are prospects for improving the sensitivity of these sensors by more than an order of magnitude to reach field resolution in the femto-Tesla range. In the following we address several routes for improved resolution: (a) increasing the signal (b) increasing the measured field and (c) decreasing the noise.

There are two main ways to increase the signal. The AMR ratio of the used Permalloy films in on the order of 1-2%. However, based on reports in the literature, optimization of deposition condition may reasonably yield an improvement of at least a factor of 2. We note that the equivalent magnetic noise is inversely proportional to the AMR ratio. Another way to increase the signal is by reducing the excess anisotropy Hex which sets a lower bound for the total effective uniaxial anisotropy. The origin of the excess anisotropy is not fully understood at this stage. We believe that it is related to internal intrinsic magnetocrystalline anisotropy which can be suppressed by the optimization process of the growth conditions. We note that Equation 4.16 equivalent magnetic noise is proportional to $\sqrt{H_{ea}}$.

The amplification of the field is commonly achieved by using magnetic flux concentrators. In the case of elliptical PHE sensors the integration of such concentrators is relatively simple. We note that flux concentrators have been used to increase to applied field by more than an order of magnitude.

The decrease of the noise can be achieved in several ways: by optimizing the sensor geometrical parameters including the parameters of the current and voltage leads and by optimizing the measuring method (amplitude and frequency of the excitation current, amplifying electronics, etc.). Based on the above, even without exploring other material systems, a low frequency femto tesla resolution with the elliptical PHE sensors is within reach. In addition to the field resolution advantage of these sensors, there are other important advantages. They are simpler than the AMR sensors; their anisotropy is tailored by shape which enables the simple fabrication on the same chip of sensors with easy axes which differ in their orientation and the strength of the effective anisotropy field. Furthermore, they are quite robust and stable a feature which decreases considerably the need to "refresh" the sensor. These features of the sensors make them suitable for a wide range of applications. They may compete with the low-cost low-resolution magnetic sensors such as Hall sensors, which are widely used in the industry; e.g., the vehicle industry. Currently, it appears that this industry does not need the improved resolution; however, it could be that once cheap high-resolution sensors are available, the need will also arise.

7. Bibliography.

[1] Y. Nagaoka, "Ferromagnetism in a Narrow, Almost Half-Filled s Band," *Physical Review,* vol. 147, pp. 392-405, 07/08/ 1966.

[2] B. D. Cullity, "Introduction to magnetic materials," 1972.

[3] T. R. McGuire and R. I. Potter, "Anisotropic magnetoresistance in ferromagnetic 3d alloys," *Magnetics, IEEE Transactions on,* vol. 11, pp. 1018-1038, 1975.

[4] W.-Y. Lee, M. F. Toney, P. Tameerug, E. Allen, and D. Mauri, "High magnetoresistance permalloy films deposited on a thin NiFeCr or NiCr underlayer," *Journal of Applied Physics,* vol. 87, pp. 6992-6994, 2000.

[5] S. Wang, T. Gao, C. Wang, and J. He, "Studies of anisotropic magnetoresistance and magnetic property of Ni81Fe19 ultra-thin films with the lower base vacuum," *Journal of Alloys and Compounds,* vol. 554, pp. 405-407, 3/25/ 2013.

[6] S. Wang, C. Wang, Y. Gao, T. Gao, G. Hu, and H. Zhang, "Anisotropic magnetoresistance of Ni81Fe19 films on NiFeNb buffer layer," *Journal of Alloys and Compounds,* vol. 575, pp. 419-422, 10/25/ 2013.

[7] W. Y. Lee, M. F. Toney, and D. Mauri, "High magnetoresistance in sputtered Permalloy thin films through growth on seed layers of (Ni0.81/Fe0.19)[1-x]Crx," *Magnetics, IEEE Transactions on,* vol. 36, pp. 381-385, 2000.

[8] T. G. S. M. Rijks, R. Coehoorn, M. J. M. de Jong, and W. J. M. de Jonge, "Semiclassical calculations of the anisotropic magnetoresistance of NiFe-based thin films, wires, and multilayers," *Physical Review B,* vol. 51, pp. 283-291, 01/01/ 1995.

[9] L. Ejsing, M. F. Hansen, A. K. Menon, H. A. Ferreira, D. L. Graham, and P. P. Freitas, "Planar Hall effect sensor for magnetic micro- and nanobead detection," *Applied Physics Letters,* vol. 84, pp. 4729-4731, 2004.

[10] I. Genish, Y. Shperber, N. Naftalis, G. Salitra, D. Aurbach, and L. Klein, "The effects of geometry on magnetic response of elliptical PHE sensors," *Journal of Applied Physics,* vol. 107, p. 09E716, 2010.

[11] V. Mor, M. Schultz, O. Sinwani, A. Grosz, E. Paperno, and L. Klein, "Planar Hall effect sensors with shape-induced effective single domain behavior," *Journal of Applied Physics,* vol. 111, Apr 1 2012.

[12] A. Grosz, V. Mor, E. Paperno, S. Amrusi, I. Faivinov, M. Schultz*, et al.*, "Planar Hall Effect Sensors With Subnanotesla Resolution," *Magnetics Letters, IEEE,* vol. 4, pp. 6500104-6500104, 2013.

[13] S. Ripka and P. Ripka, "Magnetic Sensors," in *Modern Sensors Handbook*, ed: ISTE, 2010, pp. 433-475.

[14] M. N. Baibich, J. M. Broto, A. Fert, F. N. Van Dau, F. Petroff, P. Etienne*, et al.*, "Giant Magnetoresistance of (001)Fe/(001)Cr Magnetic Superlattices," *Physical Review Letters,* vol. 61, pp. 2472-2475, 11/21/ 1988.

[15] G. Binasch, P. Grünberg, F. Saurenbach, and W. Zinn, "Enhanced magnetoresistance in layered magnetic structures with antiferromagnetic interlayer exchange," *Physical Review B,* vol. 39, pp. 4828-4830, 03/01/ 1989.

[16] P. W. Anderson, "Localized Magnetic States in Metals," *Physical Review,* vol. 124, pp. 41-53, 10/01/ 1961.

[17] N. F. Mott, "The Resistance and Thermoelectric Properties of the Transition Metals," *Proceedings of the Royal Society of London. Series A, Mathematical and Physical Sciences,* vol. 156, pp. 368-382, 1936.

[18] E. Y. Tsymbal and D. G. Pettifor, "Perspectives of giant magnetoresistance," in *Solid State Physics*. vol. Volume 56, E. Henry and S. Frans, Eds., ed: Academic Press, 2001, pp. 113-237.

[19] M. Julliere, "Tunneling between ferromagnetic films," *Physics Letters A,* vol. 54, pp. 225-226, 1975/09/08 1975.
[20] J. S. Moodera, L. R. Kinder, T. M. Wong, and R. Meservey, "Large Magnetoresistance at Room Temperature in Ferromagnetic Thin Film Tunnel Junctions," *Physical Review Letters,* vol. 74, pp. 3273-3276, 04/17/ 1995.
[21] T. Miyazaki and N. Tezuka, "Giant magnetic tunneling effect in Fe/Al2O3/Fe junction," *Journal of Magnetism and Magnetic Materials,* vol. 139, pp. L231-L234, 1/2/ 1995.
[22] R. Matsumoto, A. Fukushima, K. Yakushiji, S. Nishioka, T. Nagahama, T. Katayama*, et al.*, "Spin-dependent tunneling in epitaxial Fe/Cr/MgO/Fe magnetic tunnel junctions with an ultrathin Cr(001) spacer layer," *Physical Review B,* vol. 79, p. 174436, 05/29/ 2009.
[23] C. Chappert, A. Fert, and F. N. Van Dau, "The emergence of spin electronics in data storage," *Nat Mater,* vol. 6, pp. 813-823, 11//print 2007.
[24] J. Bass and W. P. Pratt Jr, "Current-perpendicular (CPP) magnetoresistance in magnetic metallic multilayers," *Journal of Magnetism and Magnetic Materials,* vol. 200, pp. 274-289, 10// 1999.
[25] R. C. O'handley, "Modern Magnetic Materials Principles and Applications," p. 520, 1999.
[26] Q. H. Lu, R. Huang, L. S. Wang, Z. G. Wu, C. Li, Q. Luo*, et al.*, "Thermal annealing and magnetic anisotropy of NiFe thin films on n+-Si for spintronic device applications," *Journal of Magnetism and Magnetic Materials,* vol. 394, pp. 253-259, 11/15/ 2015.
[27] R. L. Stamps, "Mechanisms for exchange bias," *Journal of Physics D: Applied Physics,* vol. 33, p. R247, 2000.
[28] J. A. Osborn, "Demagnetizing Factors of the General Ellipsoid," *Physical Review,* vol. 67, pp. 351-357, 06/01/ 1945.
[29] E. M. Chudnovsky and L. Gunther, "Quantum theory of nucleation in ferromagnets," *Physical Review B,* vol. 37, pp. 9455-9459, 06/01/ 1988.
[30] E. M. Chudnovsky and L. Gunther, "Quantum Tunneling of Magnetization in Small Ferromagnetic Particles," *Physical Review Letters,* vol. 60, pp. 661-664, 02/22/ 1988.
[31] C. Tannous and J. Gieraltowski, "A Stoner-Wohlfarth model Redux: Static properties," *Physica B-Condensed Matter,* vol. 403, pp. 3563-3570, Oct 1 2008.
[32] E. C. Stoner and E. P. Wohlfarth, "A Mechanism of Magnetic Hysteresis in Heterogeneous Alloys," *Philosophical Transactions of the Royal Society of London A: Mathematical, Physical and Engineering Sciences,* vol. 240, pp. 599-642, 1948-05-04 00:00:00 1948.
[33] E. P. Wohlfarth, "Relations between Different Modes of Acquisition of the Remanent Magnetization of Ferromagnetic Particles," *Journal of Applied Physics,* vol. 29, pp. 595-596, 1958.
[34] M. A. M. Gijs, J. B. Giesbers, P. Beliën, J. W. van Est, J. Briaire, and L. K. J. Vandamme, "1/f noise in magnetic Ni80Fe20 single layers and Ni80Fe20/Cu multilayers," *Journal of Magnetism and Magnetic Materials,* vol. 165, pp. 360-362, 1// 1997.
[35] R. M. Bozorth, *Ferromagnetism*. New York: Van Nostrand, 1951.
[36] J. C. Brice and U. Pick, "The coercive force in permalloy thin films," *British Journal of Applied Physics,* vol. 16, p. 565, 1965.
[37] M. A. Russak, C. V. Jahnes, E. Klokholm, and B. Petek, "Magnetic characterization of ion-beam sputter deposited permalloy thin films," *Journal of Magnetism and Magnetic Materials,* vol. 104, pp. 1847-1850, 1992/02/02 1992.
[38] T. T. Chen and V. A. Marsocci, "The magnetoresistivity anisotropy measurements in Ni・Fe and Ni・Pd single-crystal thin films," *Solid State Communications,* vol. 10, pp. 783-786, 5/1/ 1972.

[39] T. d. Lacheisserie, "Magnetism Materials and Applications.," *Springer,* p. 282, 2005.
[40] C. Nishimura, Y. Nagai, K. Yanagisawa, and T. Toshima, "Magnetic properties of NiFe films prepared using ion-beam sputtering," *IEEE Transactions on Magnetics,* vol. 23, pp. 2728-2730, 1987.
[41] F. Pfeifer and C. Radeloff, "Soft magnetic Ni-Fe and Co-Fe alloys - some physical and metallurgical aspects," *Journal of Magnetism and Magnetic Materials,* vol. 19, pp. 190-207, 1980/04/02 1980.
[42] D. E. Heim, R. E. Fontana, Jr., C. Tsang, V. S. Speriosu, B. A. Gurney, and M. L. Williams, "Design and operation of spin valve sensors," *Magnetics, IEEE Transactions on,* vol. 30, pp. 316-321, 1994.
[43] D. A. Hall, R. S. Gaster, K. A. A. Makinwa, S. X. Wang, and B. Murmann, "A 256 Pixel Magnetoresistive Biosensor Microarray in 0.18 µm CMOS," *Solid-State Circuits, IEEE Journal of,* vol. 48, pp. 1290-1301, 2013.
[44] V. C. Martins, J. Germano, F. A. Cardoso, J. Loureiro, S. Cardoso, L. Sousa*, et al.*, "Challenges and trends in the development of a magnetoresistive biochip portable platform," *Journal of Magnetism and Magnetic Materials,* vol. 322, pp. 1655-1663, 5// 2010.
[45] T. Costa, M. S. Piedade, J. Germano, J. Amaral, and P. P. Freitas, "An instrumentation system based on magnetoresistive sensors for neuronal signal detection," in *Instrumentation and Measurement Technology Conference (I2MTC), 2013 IEEE International*, 2013, pp. 1074-1077.
[46] F. Qejvanaj, H. Mazraati, S. Jiang, A. Persson, S. R. Sani, S. Chung*, et al.*, "Planar Hall-Effect Bridge Sensor With NiFeX (X <inline-formula> <img src="/images/tex/32586.gif" alt="="> </inline-formula> Cu, Ag, and Au) Sensing Layer," *Magnetics, IEEE Transactions on,* vol. 51, pp. 1-4, 2015.
[47] A. D. Henriksen, G. Rizzi, and M. F. Hansen, "Experimental comparison of ring and diamond shaped planar Hall effect bridge magnetic field sensors," *Journal of Applied Physics,* vol. 118, p. 103901, 2015.
[48] T. Q. Hung, F. Terki, S. Kamara, K. Kim, S. Charar, and C. Kim, "Planar Hall ring sensor for ultra-low magnetic moment sensing," *Journal of Applied Physics,* vol. 117, p. 154505, 2015.
[49] N. A. Stutzke, S. E. Russek, D. P. Pappas, and M. Tondra, "Low-frequency noise measurements on commercial magnetoresistive magnetic field sensors," *Journal of Applied Physics,* vol. 97, p. 10Q107, 2005.
[50] P. Ripka and M. Janosek, "Advances in Magnetic Field Sensors," *Sensors Journal, IEEE,* vol. 10, pp. 1108-1116, 2010.
[51] F. G. West, "Rotating-Field Technique for Galvanomagnetic Measurements," *Journal of Applied Physics,* vol. 34, pp. 1171-1173, 1963.
[52] M. Volmer and M. Avram, "Using permalloy based planar hall effect sensors to capture and detect superparamagnetic beads for lab on a chip applications," *Journal of Magnetism and Magnetic Materials,* vol. 381, pp. 481-487, 5/1/ 2015.
[53] A. D. Henriksen, B. T. Dalslet, D. H. Skieller, K. H. Lee, F. Okkels, and M. F. Hansen, "Planar Hall effect bridge magnetic field sensors," *Applied Physics Letters,* vol. 97, Jul 5 2010.
[54] A. Persson, R. S. Bejhed, F. W. Osterberg, K. Gunnarsson, H. Nguyen, G. Rizzi*, et al.*, "Modelling and design of planar Hall effect bridge sensors for low-frequency applications," *Sensors and Actuators a-Physical,* vol. 189, pp. 459-465, Jan 15 2013.
[55] F. W. Osterberg, G. Rizzi, T. Z. G. de la Torre, M. Stromberg, M. Stromme, P. Svedlindh*, et al.*, "Measurements of Brownian relaxation of magnetic nanobeads using planar Hall effect bridge sensors," *Biosensors & Bioelectronics,* vol. 40, pp. 147-152, Feb 15 2013.

[56] A. Persson, R. S. Bejhed, H. Nguyen, K. Gunnarsson, B. T. Dalslet, F. W. Osterberg*, et al.*, "Low-frequency noise in planar Hall effect bridge sensors," *Sensors and Actuators a-Physical,* vol. 171, pp. 212-218, Nov 2011.

[57] S. J. Oh, T. T. Le, G. W. Kim, and C. Kim, "Size effect on NiFe/Cu/NiFe/IrMn spin-valve structure for an array of PHR sensor element," *Physica Status Solidi a-Applications and Materials Science,* vol. 204, pp. 4075-4078, Dec 2007.

[58] N. T. Thanh, K. W. Kim, O. Kim, K. H. Shin, and C. G. Kim, "Microbeads detection using Planar Hall effect in spin-valve structure," *Journal of Magnetism and Magnetic Materials,* vol. 316, pp. E238-E241, Sep 2007.

[59] B. Bajaj, N. T. Thanh, and C. G. Kim, "Planar Hall Effect in Spin Valve Structure for DNA Detection Immobilized with Single Magnetic Bead," *2007 7th Ieee Conference on Nanotechnology, Vol 1-3,* pp. 1037-1040, 2007.

[60] N. T. Thanh, B. P. Rao, N. H. Duc, and C. Kim, "Planar Hall resistance sensor for biochip application," *Physica Status Solidi a-Applications and Materials Science,* vol. 204, pp. 4053-4057, Dec 2007.

[61] S. Oh, N. S. Baek, S. D. Jung, M. A. Chung, T. Q. Hung, S. Anandakumar*, et al.*, "Selective Binding and Detection of Magnetic Labels Using PHR Sensor via Photoresist Micro-Wells," *Journal of Nanoscience and Nanotechnology,* vol. 11, pp. 4452-4456, May 2011.

[62] D. T. Bui, M. D. Tran, H. D. Nguyen, and H. B. Nguyen, "High-sensitivity planar Hall sensor based on simple gaint magneto resistance NiFe/Cu/NiFe structure for biochip application," *Advances in Natural Sciences: Nanoscience and Nanotechnology,* vol. 4, p. 015017, 2013.

[63] M. Volmer and J. Neamtu, "Micromagnetic characterization of a rotation sensor based on the planar Hall effect," *Physica B-Condensed Matter,* vol. 403, pp. 350-353, Feb 1 2008.

[64] M. Volmer, M. Avram, and A. M. Avram, "On Manipulation and Detection of Biomolecules Using Magnetic Carriers," *Cas: 2009 International Semiconductor Conference, Vols 1 and 2, Proceedings,* pp. 155-158, 2009.

[65] T. Q. Hung, S. J. Oh, B. D. Tu, N. H. Duc, L. V. Phong, S. AnandaKumar*, et al.*, "Sensitivity Dependence of the Planar Hall Effect Sensor on the Free Layer of the Spin-Valve Structure," *Ieee Transactions on Magnetics,* vol. 45, pp. 2374-2377, Jun 2009.

[66] T. Q. Hung, J. R. Jeong, D. Y. Kim, H. D. Nguyen, and C. Kim, "Hybrid planar Hall-magnetoresistance sensor based on tilted cross-junction," *Journal of Physics D-Applied Physics,* vol. 42, Mar 7 2009.

[67] B. D. Tu, L. V. Cuong, T. Q. Hung, D. T. H. Giang, T. M. Danh, N. H. Duc*, et al.*, "Optimization of Spin-Valve Structure NiFe/Cu/NiFe/IrMn for Planar Hall Effect Based Biochips," *Ieee Transactions on Magnetics,* vol. 45, pp. 2378-2382, Jun 2009.

[68] B. Sinha, S. Anandakumar, S. Oh, and C. Kim, "Micro-magnetometry for susceptibility measurement of superparamagnetic single bead," *Sensors and Actuators a-Physical,* vol. 182, pp. 34-40, Aug 2012.

[69] M. Volmer and J. Neamtu, "Electrical and micromagnetic characterization of rotation sensors made from permalloy multilayered thin films," *Journal of Magnetism and Magnetic Materials,* vol. 322, pp. 1631-1634, May-Jun 2010.

[70] M. Volmer and J. Neamtu, "Magnetic field sensors based on Permalloy multilayers and nanogranular films," *Journal of Magnetism and Magnetic Materials,* vol. 316, pp. E265-E268, Sep 2007.

[71] T. Q. Hung, B. P. Rao, and C. Kim, "Planar Hall effect in biosensor with a tilted angle of the cross-junction," *Journal of Magnetism and Magnetic Materials,* vol. 321, pp. 3839-3841, Dec 2009.

[72] Z. Q. Lu and G. Pan, "Spin valves with spin-engineered domain-biasing scheme," *Applied Physics Letters,* vol. 82, pp. 4107-4109, Jun 9 2003.
[73] B. D. Tu, L. V. Cuong, T. H. G. Do, T. M. Danh, and N. H. Duc, "Optimization of planar Hall effect sensor for magnetic bead detection using spin-valve NiFe/Cu/NiFe/IrMn structures," *Apctp-Asean Workshop on Advanced Materials Science and Nanotechnology (Amsn08),* vol. 187, 2009.
[74] T. Q. Hung, S. Oh, J. R. Jeong, and C. Kim, "Spin-valve planar Hall sensor for single bead detection," *Sensors and Actuators a-Physical,* vol. 157, pp. 42-46, Jan 2010.
[75] M. Volmer and J. Neamtu, "Optimisation of Spin-Valve Planar Hall Effect Sensors for Low Field Measurements," *Ieee Transactions on Magnetics,* vol. 48, pp. 1577-1580, Apr 2012.
[76] K. M. Chui, A. O. Adeyeye, and M. H. Li, "Detection of a single magnetic dot using a Planar Hall sensor," *Journal of Magnetism and Magnetic Materials,* vol. 310, pp. E992-E993, Mar 2007.
[77] M. Volmer and J. Neamtu, "Micromagnetic analysis and development of high sensitivity spin-valve magnetic sensors," *5th International Workshop on Multi-Rate Processes and Hysteresis (Murphys 2010),* vol. 268, 2010.
[78] C. Christides, S. Stavroyiannis, and D. Niarchos, "Enhanced planar Hall voltage changes measured in Co/Cu multilayers and Co films with square shapes," *Journal of Physics-Condensed Matter,* vol. 9, pp. 7281-7290, Sep 1 1997.
[79] K. M. Chui, A. O. Adeyeye, and M.-H. Li, "Effect of seed layer on the sensitivity of exchange biased planar Hall sensor," *Sensors and Actuators A: Physical,* vol. 141, pp. 282-287, 2/15/ 2008.
[80] T. Q. Hung, S. Oh, B. Sinha, J. R. Jeong, D. Y. Kim, and C. Kim, "High field-sensitivity planar Hall sensor based on NiFe/Cu/IrMn trilayer structure," *Journal of Applied Physics,* vol. 107, May 1 2010.
[81] S. Oh, S. Anandakumar, C. Lee, K. W. Kim, B. Lim, and C. Kim, "Analytes kinetics in lateral flow membrane analyzed by cTnI monitoring using magnetic method," *Sensors and Actuators B-Chemical,* vol. 160, pp. 747-752, Dec 15 2011.
[82] S. Oh, P. B. Patil, T. Q. Hung, B. Lim, M. Takahashi, D. Y. Kim*, et al.*, "Hybrid AMR/PHR ring sensor," *Solid State Communications,* vol. 151, pp. 1248-1251, Sep 2011.
[83] F. Qejvanaj, M. Zubair, A. Persson, S. M. Mohseni, V. Fallahi, S. R. Sani*, et al.*, "Thick Double-Biased IrMn/NiFe/IrMn Planar Hall Effect Bridge Sensors," *Magnetics, IEEE Transactions on,* vol. 50, pp. 1-4, 2014.
[84] B. Sinha, T. Quang Hung, T. Sri Ramulu, S. Oh, K. Kim, D.-Y. Kim*, et al.*, "Planar Hall resistance ring sensor based on NiFe/Cu/IrMn trilayer structure," *Journal of Applied Physics,* vol. 113, p. 063903, 2013.
[85] T. Musha, "Physical background of Hooge's α for 1/f noise," *Physical Review B,* vol. 26, pp. 1042-1043, 07/15/ 1982.
[86] M. Lakshmanan, "The fascinating world of the Landau–Lifshitz–Gilbert equation: an overview," *Philosophical Transactions of the Royal Society of London A: Mathematical, Physical and Engineering Sciences,* vol. 369, pp. 1280-1300, 2011-03-28 00:00:00 2011.
[87] M. D. Donahue and D. Porter, "OOMMF http://math.nist.gov/oommf/."

Planar Hall effect sensors with shape-induced effective single domain behavior

V. Mor,[1,a)] M. Schultz,[1] O. Sinwani,[1] A. Grosz,[2] E. Paperno,[2] and L. Klein[1]
[1]*Department of Physics, Nano-magnetism Research Center, Institute of Nanotechnology and Advanced Materials, Bar-Ilan University, Ramat-Gan 52900, Israel*
[2]*Department of Electrical and Computer Engineering, Ben-Gurion University of the Negev, P.O. Box 653, Beer-Sheva 84105, Israel*

(Presented 1 November 2011; received 23 September 2011; accepted 21 December 2011; published online 13 March 2012)

We show that shape anisotropy induces effective single domain behavior in elliptical structures of thin permalloy films with long axis ranging between several microns to several millimeters, provided that the ratio of the film long and short axes is large enough. We also show that the thin film elliptical structures exhibit a wide range of effective anisotropy fields, from less than 10 Oe up to more than 100 Oe. We discuss the advantage of shape anisotropy in the fabrication of planar Hall effect sensors with high field resolution. © *2012 American Institute of Physics*. [doi:10.1063/1.3680084]

The longitudinal and transverse resistivities of polycrystalline ferromagnetic films, for which the crystal symmetry effects are averaged out, depend on the angle θ between the electric current (**J**) and the magnetization (**M**) as follows:

$$\rho_{xx} = \rho_{\perp} + (\rho_{\parallel} - \rho_{\perp})\cos^2\theta, \tag{1}$$

$$\rho_{xy} = \frac{1}{2}(\rho_{\parallel} - \rho_{\perp})\sin 2\theta, \tag{2}$$

where $\rho_{\parallel}$ and $\rho_{\perp}$ are the resistivities parallel and perpendicular to the magnetization, respectively. Equation (1) describes the anisotropic magnetoresistance effect, whereas Eq. (2) describes the planar Hall effect (PHE).[1,2]

Magnetic sensors based on PHE usually use patterned magnetic films with effective single domain behavior. This is usually achieved by growth-induced magnetic anisotropy, either by growing the film in a magnetic field[3] or by exchange biasing the film with an antiferromagnetic layer.[4,5] These methods yield a single easy axis of magnetization that aligns the magnetization with the current when no field is applied. When a field perpendicular to the easy axis (in the film plane) is applied, the magnetization rotates uniformly and reversely. The change in ρ_{xy} due to this rotation is used to detect the magnitude of the component of the field which is perpendicular to the easy axis.

Here we show that shape anisotropy can be reliably used for achieving effective single domain behavior. Moreover, this method has unique advantages in the design of sensing devices based on the PHE. We also show that shape induced anisotropy can be approximated analytically and that single domain behavior can be induced in a very wide range of parameters provided the axes ratio of the ellipses is large enough.

To manufacture the sensors, we sputter permalloy films capped with tantalum on Si substrates in an UHV-evaporation and sputtering system (BESTEC). We pattern the elliptical sensors with an e-beam high resolution lithography system (CRESTEC) using either lift-off or Ar^+ milling. Leads and contact pads are deposited in a second stage. Figure 1 shows one of the sensors whose performance is reported here. Response measurements are performed using a Helmholtz coils system with a rotating sample stage having an angle resolution of 0.03^o. The sample is connected electrically to a switch box (Keithley 7001), a current source (Keithley 2400), and a nanovoltmeter (Keithley 2182). Sensitivity threshold (equivalent magnetic noise) measurements are performed at 1 Hz with the experimental setup shown in Fig. 2.

Figure 3 presents two types of experiments that demonstrate the effective single domain behavior of our elliptical sensors. The dimensions of the ellipse are 2 mm length, 0.25 mm width, and 60 nm thickness. Figure 3(a) shows the normalized PHE measured across the permalloy ellipse as a function of the angle α between **H** and ***J***. **J** is applied along the ellipse long axis. For each angle, the voltage is measured twice: with H = 100 Oe (the filled symbols) and H = 0 (the unfilled symbols). The voltage measured in the latter case indicates that for each α, **M** fully returns to the easy axis, and the variations in the zero-field signals are consistent with the expected effect of a small ambient field.

Figure 3(b) shows a sharp switching behavior of the measured PHE as a function of **H** at $\alpha = 130^o$ relative to the long axis of the ellipse. This type of behavior indicates effective single domain behavior with effective uniaxial anisotropy along the long axis of the ellipse, which is usually described by the Stoner–Wohlfarth Hamiltonian,

$$\mathcal{H} = K_u \sin^2\theta - M_s H\cos(\alpha - \theta), \tag{3}$$

where M_s is the saturation magnetization, K_u is the magnetic anisotropy constant, θ is the angle between M_s and the easy axis, and α is the angle between the external magnetic field **H** and the easy axis.

a)Author to whom correspondence should be addressed. Electronic mail: vladislav.mor@gmail.com.

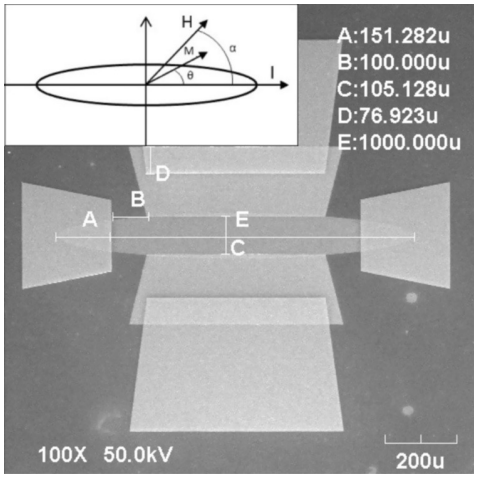

FIG. 1. Scanning electron microscope image of a typical PHE sensor. The elliptical part is made of permalloy capped with tantalum. Current is driven along the long axes through gold leads connected to the contact leads. Voltage is measured via the tantalum and gold leads connected to the contact pads. The inset shows the directions of the magnetic field (**H**) and the magnetization **M** relative to the current (**I**).

Figure 3(d) shows the dependence of the switching field (H_s) on α. The line is the expected for coherent rotation[6]

$$H_s(\alpha) = \frac{H_k}{\left[\sin^{2/3}\alpha + \cos^{2/3}\alpha\right]^{3/2}}, \tag{4}$$

where H_k is the anisotropy field defined as $2K_u/M_s$. We note that for α close to 180° the experimental points deviate from the theoretical prediction, indicating that in this narrow range of angles the magnetization reversal cannot be described in terms of coherent rotation. This, however, does not affect the functionality of our sensors, which are used to detect fields much smaller than the anisotropy field.

To determine the effective H_k of our sensors, we apply a small field perpendicular to the easy axis and measure the slope of θ versus $H_\perp$. Figure 4 represents the experimentally extracted H_k for elliptical sensors in a wide range of sizes as a function of c/b, where c is the film thickness, and b is the short axis of the ellipse.

We compare now the observed behavior with that of an ellipsoid of similar dimensions whose response can be studied analytically. For ellipsoids, one can define and calculate demagnetization factors, which have the following form in the limit $a \geq b \gg c$:[7]

$$\frac{N_a}{4\pi} = \frac{c}{a}(1-e^2)^{1/2}\frac{K-E}{e^2}, \tag{5}$$

$$\frac{N_b}{4\pi} = \frac{c}{a}\frac{E-(1-e^2)K}{e^2(1-e^2)^{1/2}}, \tag{6}$$

$$\frac{N_c}{4\pi} = 1 - \frac{E}{a(1-e^2)^{1/2}}, \tag{7}$$

where a, b, and c are the axes of the ellipsoid. N_a, N_b, and N_c are the demagnetizing factors (corresponding to a, b, and c respectively). K is a complete elliptic integral of the first kind and E is a complete elliptic integral of the second kind,

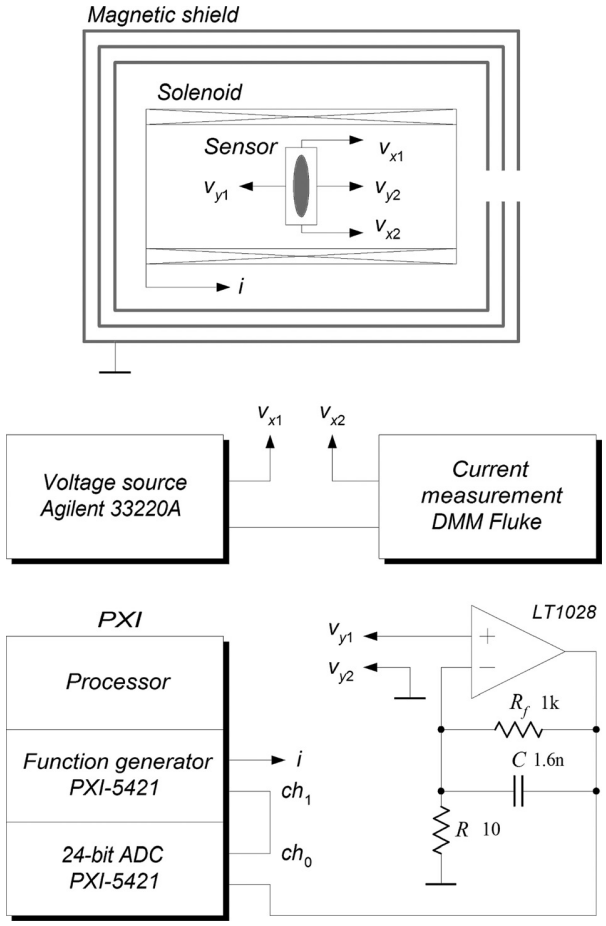

FIG. 2. Experimental setup for measuring the sensor resolution. The setup includes a three-shell magnetic shield, a voltage source, a current measurement instrument (to apply a bias), a preamplifier, and a National Instruments personal computer-based platform for test, measurement, and control (PXI).

whose argument is $e = (1 - b^2/a^2)^{1/2}$. The behavior of the sensors when **H** is applied in the *ab* plane can be described by the Stoner–Wohlfarth Hamiltonian where the anisotropy constant K_u is given by $K_u = (1/2)M_s^2(N_b - N_a)$.

In the limit $a \gg b \gg c$ we use the asymptotic expansions of K and E (Ref. 8) to obtain

$$H_k \sim 4\pi M_s \frac{c}{b} \sim 10,807\frac{c}{b}Oe. \tag{8}$$

We compare the analytical approximation with the experimental results (see Fig. 4) and note that the experimental value of H_k has a lower bound. This is due to the effect of the intrinsic anisotropy of the permalloy film, which is growth dependent and usually varies between 5 and 10 Oe. We compare the analytical approximation with OOMMF (Ref. 9) simulations and note that the approximation in Eq. (8) is quite good for $a/b \geq 8$.

We have also performed simulations for ellipses and rectangles and have found that the analytical approximation is better for elongated ellipses.

The simulations also indicate the effective single domain behavior for ellipsoids and ellipses in a very wide range of sizes, whereas rectangular samples are much less stable. The ellipses with axes ratio of 6 : 1 and above behave quite

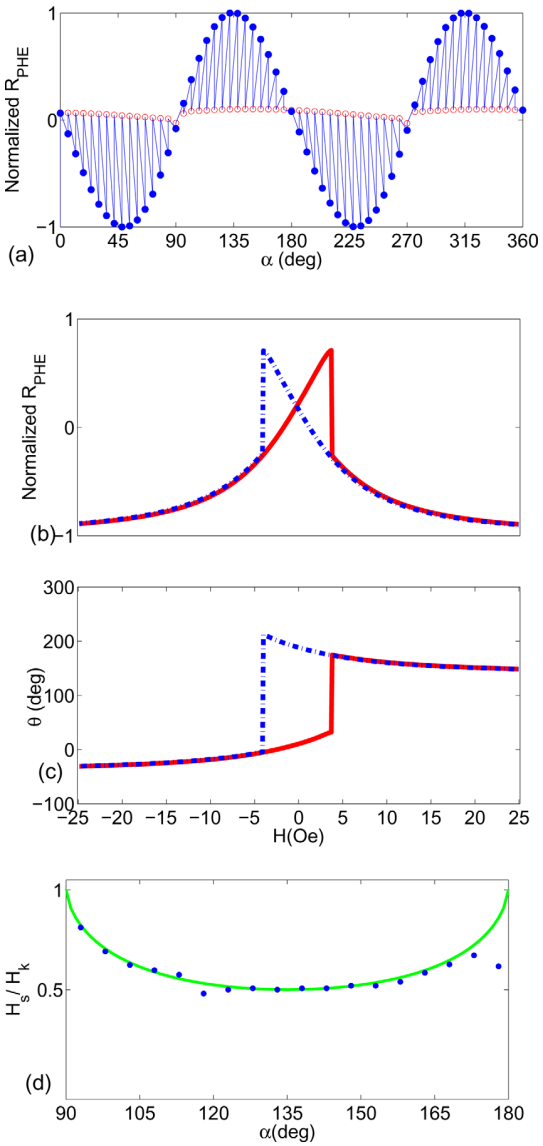

FIG. 3. (Color online) Effective single-domain behavior of large elliptical sensors. (a) Normalized PHE measured across an elliptical sensor as a function of the angle α between **H** and **J**. The dimensions of the ellipse are 2 mm length, 0.25 mm width, and 60 nm thickness, and **J** is applied along its long axis. For each α, the voltage is measured twice: with H = 100 Oe (filled symbols) and with H = 0 (unfilled symbols). (b)The PHE as a function of **H** at an angle $\alpha = 130^{o}$ for elliptical sensor with dimensions 1 mm length, 0.125 mm width, and 60 nm thickness. (c) The corresponding θ for the measurements shown in b. (d) The switching field divided by H_k as a function of α. The line is a fit to the Stoner–Wohlfart model.

like a single domain particle and the behavior improves with increasing axes ratio.

Surprisingly, the single-domain-like behavior is observed even for very large ellipses. This has a practical importance since the big ellipses have a very small H_k, which means that their sensitivity $S = (V_{\mathrm{PHE}}/I)(1/H_{\perp}) \propto 1/H_k$ is higher. Here, V_{PHE} is the measured transverse voltage, I is the current through the sensor, $H_{\perp}$ is the field applied perpendicular to the easy axis. We have obtained H_k as small as 8 Oe and S as big as 200 Ω/T.

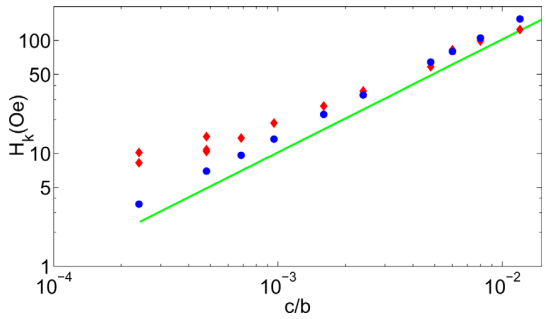

FIG. 4. (Color online) The experimental (diamonds) and simulated (dots) shape anisotropy field for ellipses as a function of the axes ratio b/c. The line represents the theoretical anisotropy field of ellipsoids [Eq. (8)].

The field resolution of our sensors is determined using the setup described in Fig. 2. First, we measure the sensitivity of sensor. Second, we measure the amplitude spectral density of the noise, and then translate the noise spectral density into the sensitivity threshold by dividing it by the sensitivity.

To measure the sensitivity, we apply an external magnetic field by a long solenoid connected to a function generator, bias the sensor with a voltage source, amplify the sensor output by an ultra-low noise preamplifier, and sample the preamplifier output by a 24 bit analog to digital convertor. The amplifier noise is negligible compared to the 1/f noise of the sensor at a given ac bias current, and there is no need to use either Wheatstone Bridge or cross-correlation techniques. All the measurements are performed in a three-layer magnetic shield. Using this setup, we find that our best sensors have at 1 Hz field resolution of about 0.6 $nT/\sqrt{Hz}$.

We believe that H_k can be further reduced by more than an order of magnitude, which would increase S accordingly. In addition, a flux concentrator can be used to amplify the measured field.[10,11] Therefore, it appears likely that further improvement of the field resolution by orders of magnitude is within reach.

Such sensors could be very useful for applications not only for their high resolution but also because they offer the possibility of fabricating on a single device, multiple sensors with a wide range of H_k along different directions—features that open new opportunities for PHE sensors.

L.K. acknowledges support by the Israel Science Foundation founded by the Israel Academy of Science and Humanities. The content of this manuscript is patent pending.

[1]C. Goldberg and R. E. Davis, Phys. Rev. **94**, 1121 (1954).
[2]F. G. West, J. Appl. Phys. **34**, 1171 (1963).
[3]A. Schuhl, F. N. Van Dau, and J. R. Childress, Appl. Phys. Lett. **66**, 2751 (1995).
[4]C. D. Damsgaard *et al.*, Sens. Actuators, A **56**, 103 (2009).
[5]A. Nemoto, Appl. Phys. Lett.**74**, 4026 (1999).
[6]C. Tannous and J. Gieraltowski, Eur. J. Phys. **29**, 475 (2008).
[7]J. A. Osborn, Phys. Rev. **67**, 351 (1945).
[8]A. Gasull *et al.*, Pac. J. Math. **202**, 341 (2002).
[9]The publicly available object oriented micromagnetic framework, http://math.nist.gov/oommf.
[10]F. Montaigne *et al.*, Sens. nd Actuators, A **81**, 324 (2000).
[11]F. N. Van Dau *et al.*, The 8th International Conference on Solid-State Sensors and Actuators, and Eurosensors IX, Transducers '95, Stockholm, Sweden, June 25–29, 1995, p. 292.

Magnetic Instruments

Planar Hall Effect Sensors With Subnanotesla Resolution

A. Grosz[1], V. Mor[2], E. Paperno[1], S. Amrusi[1], I. Faivinov[1], M. Schultz[2], and L. Klein[2]

[1]*Department of Electrical and Computer Engineering, Ben-Gurion University of the Negev, P.O. Box 653, Beer-Sheva 84105, Israel*
[2]*Department of Physics, Institute of Nanotechnology and Advanced Materials, Bar-Ilan University, Ramat-Gan 52900, Israel*

Received 20 June 2013, revised 19 July 2013, accepted 29 July 2013, published 26 August 2013.

Abstract—We report the fabrication of elliptical planar Hall effect sensors made of Permalloy with response determined by shape-induced uniaxial anisotropy. By using ac excitation and by optimizing the sensor thickness and the amplitude of the excitation current, we have obtained a magnetic field resolution which is better than 600 pT/$\sqrt{}$Hz at 1 Hz and close to 1 nT /$\sqrt{}$Hz at 0.1 Hz. We discuss possible routes for further improvement of the obtained resolution.

Index Terms—Magnetic instruments, magnetic sensors, planar Hall effect, resolution, sensor, subnanotesla.

I. INTRODUCTION

Among the wide range of magnetic sensors, those based on magnetoresistance (MR) effects are particularly attractive as they combine low cost, small size, and relatively high resolution at room temperature. To date, within the group of MR sensors, anisotropic magnetoresistance (AMR) sensors [Stutzke 2005] hold the best resolution of 200 pT/$\sqrt{}$Hz at 1 Hz. Other promising results were obtained for example by using an ensemble of tunneling magnetoresistance (TMR) sensors [Liou 2011] or by the integration of MEMS flux concentrators [Hu 2013].

Planar Hall effect (PHE) sensors [Mor 2012, Persson 2013, Schuhl 1995] have important intrinsic advantages compared to AMR sensors. PHE sensors are less sensitive to temperature drift [Schuhl 1995], which limits the resolution at low frequencies. They are also much simpler compared to TMR or giant magnetoresistance sensors, which comprise a stack of layers fabricated in complex processes. Such a layer stack also results in additional sources of noise, which is difficult to control and suppress [Lei 2011].

Despite the advantages, so far the reported resolution of PHE sensors is lower than that of AMR sensors [Stutzke 2005], [Honeywell 2008]: 2 nT/$\sqrt{}$Hz at 1 Hz for the best PHE sensor in bridge configuration (PHEB) [Persson 2013] and even worse in regular PHE sensors [Montaigne 2000]. However, as we show in this letter, PHE sensors can approach the resolution of AMR sensors at 1 Hz and surpass it at frequencies below 0.2 Hz. Furthermore, we point out routes that may further improve the resolution.

We also show in this letter that compared to miniature CMOS microfluxgates of comparable size and Hall effect sensors [Ripka 2010], the resolution of PHE sensors can be higher by one and three orders of magnitude, respectively.

To develop PHE sensors with improved resolution, we take the following approach: 1) we use an ac excitation current to translate the sensor output signal to frequencies where the $1/f$ noise of the electronic preamplifier can be neglected, 2) guided by an analytical model, we optimize the thickness of the magnetic layer, and 3) we optimize the amplitude of the excitation current.

II. SENSOR TECHNOLOGY

A PHE sensor is usually fabricated so that in zero applied magnetic field, the magnetization is parallel to the excitation current, flowing along the long sensor axis. This can be achieved via growth-induced magnetic anisotropy, either by growing the film in an applied magnetic field [Schuhl 1995] or by exchange biasing the film with an antiferromagnetic layer [Nemoto 1999]. These methods yield a single easy axis of magnetization, and consequently, uniform magnetization and its coherent rotation, when an in-plane magnetic field is applied perpendicular to the sensor easy axis.

Here, we use shape-induced anisotropy of elongated ellipses (see Fig. 1) to obtain anisotropy fields smaller than 10 Oe. The small anisotropy field increases the sensitivity of the sensor which reduces its equivalent magnetic noise.

We sputter Permalloy ($Ni_{80}Fe_{20}$) films capped with tantalum on Si substrates in a UHV evaporation and sputtering system (BESTEC). We pattern the elliptical sensors using

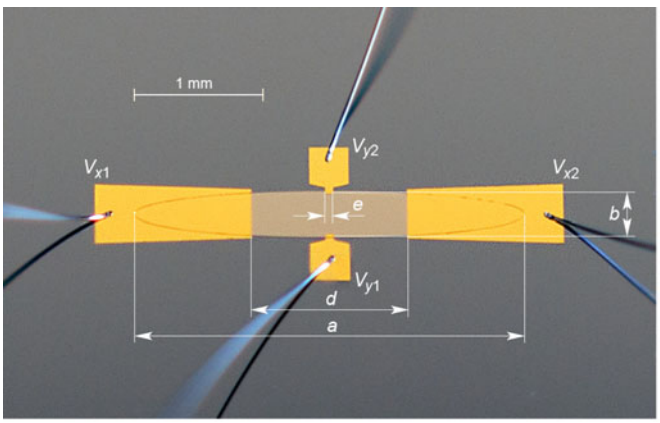

Fig. 1. Photograph of the PHE sensor. The elliptical part is made of Permalloy capped with tantalum. Excitation current is applied via the V_x gold terminals, and the output voltage is measured at the V_y terminals.

Corresponding author: A. Grosz (asaf.grosz@gmail.com).
Digital Object Identifier: 10.1109/LMAG.2013.2276551

photolithography in a liftoff process. Gold leads and contact pads are deposited in the second stage.

It was shown [Mor 2012] that elongated ellipses with aspect ratio $a/b > 6$ behave as single magnetic domain particles with effective anisotropy field along the long axis even in relatively large ellipses with long axes in the millimeter range. Although it becomes more challenging as the probability of detrimental film imperfections in the ellipse increases with size.

The single magnetic domain behavior keeps the sensor gain stable and reproducible over time and also considerably reduces its $1/f$ noise [Gijs 1997].

III. SENSOR MODEL

In polycrystalline ferromagnetic films, where crystal symmetry effects are averaged out, the longitudinal and transverse resistivities depend on the angle θ between the excitation current and the sensor magnetization as follows:

$$\rho_{xx} = \rho_{\perp} + \Delta\rho \cos^2\theta \tag{1}$$

$$\rho_{xy} = \frac{1}{2}\Delta\rho \sin 2\theta \tag{2}$$

where $\Delta\rho = \rho_{||} - \rho_{\perp}$, $\rho_{||}$ and $\rho_{\perp}$ are the resistivities parallel and perpendicular to the magnetization, respectively.

Equation (1) describes the AMR effect, whereas (2) describes the PHE.

The PHE resistivity is sensitive only to $\Delta\rho$, whereas the AMR resistivity is sensitive also to the resistivity and its temperature dependence [Schuhl 1995].

The sensitivity of a PHE sensor when the applied magnetic field is smaller than the magnetic anisotropy can be expressed as follows [Ejsing 2006]:

$$S_y = \frac{V_y}{B} = 10^4 \frac{V_x}{R_x} \cdot \frac{\Delta\rho}{t} \cdot \frac{1}{H_k + H_a} \tag{3}$$

where V_y is the sensor output voltage, measured across the y-terminals, B is the applied magnetic field, V_x is the bias voltage across the x-terminals, R_x is the sensor resistance across the x-terminals, ρ is the sensor average electrical resistivity, t is the sensor thickness, H_k is the sensor shape induced anisotropy field, and H_a is the intrinsic anisotropy field.

The total noise of a PHE sensor has three main components (see Fig. 2): $1/f$ noise, thermal noise, and preamplifier noise.

$$e_{\sum} = \sqrt{V_x^2 \frac{\delta_H}{N_C \cdot \mathrm{Vol} \cdot f^{\alpha}} + 4k_B T R_y + e_{\mathrm{amp}}^2} \tag{4}$$

where δ_H is the Hooge constant [Gijs 1997], N_C is the "free" electron density, equal to $1.7 \times 10^{29}\ 1/m^3$ for $Ni_{80}Fe_{20}$ Permalloy [Gijs 1997], Vol is the effective volume, where the electrons are contributing to the conduction process in a homogeneous sample [Gijs 1997], f is the frequency, α is a constant, k_B is the Boltzmann constant, T is the temperature, R_y is the sensor resistance across the y-terminals, and e_{amp} is the total preamplifier noise, referred to its input (including the voltage noise, current noise, and the noise of the resistors).

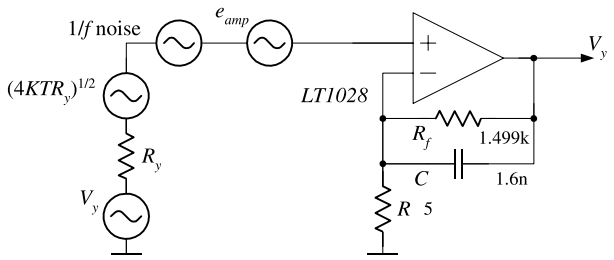

Fig. 2. Equivalent electrical circuit of the PHE sensor.

The sensor equivalent magnetic noise is defined as

$$B_{\mathrm{eq}} = \frac{e_{\sum}}{S_y}. \tag{5}$$

For sufficiently low f and high V_x, the $1/f$ noise in (4) dominates, and the other noise components can be neglected. Consequently

$$B_{\mathrm{eq}} = \sqrt{\frac{\delta_H}{N_C \cdot \mathrm{Vol} \cdot f^{\alpha}}} \frac{(H_k + H_a) \cdot t \cdot R_x}{10^4 \cdot \Delta\rho}. \tag{6}$$

For our elliptical sensors, in the limit [Mor 2012], $a > b \gg t$

$$H_k \approx 10,807 \frac{t}{b} \approx 10^4 \frac{t}{b}. \tag{7}$$

We turn now to the approximation of R_x, Vol, and R_y, assuming $t \ll a, b, d$, and e (see Fig. 1) that is valid for our sensors.

We approximate R_x by

$$R_x = \frac{C_1 \cdot \rho \cdot d}{t \cdot b} \tag{8}$$

where we expect C_1 to be a constant not much larger than 1. Assuming that the relevant volume for Vol is an effective volume that contributes to the measured transverse voltage V_y, we approximate

$$\mathrm{Vol} = C_2 \cdot t \cdot b \cdot e \tag{9}$$

$$R_y = \frac{C_3 \cdot \rho \cdot b}{t \cdot e \cdot C_2} \tag{10}$$

where C_3 similarly to C_1 is a constant not much larger than 1. These constants are due to the interface resistance between the gold and Permalloy films, which increases the total value of R_x and R_y. C_2 is a constant larger than 1 that relates the real, rectangle shaped volume between the y-terminals to the effective conduction volume.

We note that in our analysis, we consider H_a, $\Delta\rho/\rho$, and ρ to be constants, which is justified for the range of thicknesses relevant for our sensors.

Equation (6) represents the minimum equivalent magnetic noise, because increasing V_x increases the sensor sensitivity in (3) and also, as mentioned previously, the $1/f$ noise in (4) relative to the sensor thermal noise and the noise of the preamplifier, thus making them negligible.

By substituting (7)–(9) into (6), we obtain

$$B_{\text{eq}} = \sqrt{\frac{\delta_H}{N_C \cdot C_2 \cdot t \cdot b \cdot e \cdot f^{\alpha}}} \frac{\left(10^4 t + b \cdot H_a\right) \cdot C_1 \cdot d \cdot \rho}{10^4 \cdot \Delta\rho \cdot b^2}. \quad (11)$$

It is important to note that the equivalent magnetic noise in (11) depends only on the sensor dimensions and the material properties.

The optimal sensor thickness that minimizes (11) is

$$t_{\text{opt}} = \frac{H_a \cdot b}{10^4}. \quad (12)$$

Interestingly, for this thickness

$$H_k \approx H_a. \quad (13)$$

By substituting (12) into (11), we obtain the sensor low-frequency equivalent magnetic noise at the optimal thickness

$$B_{\min} = \sqrt{\frac{\delta_H}{N_C \cdot C_2 \cdot e \cdot f^{\alpha}}} \frac{2\sqrt{H_a} \cdot C_1 \cdot d \cdot \rho}{10^2 \cdot \Delta\rho \cdot b^2}. \quad (14)$$

IV. EXPERIMENT

Guided by the aforementioned considerations, we have fabricated PHE sensors with aspect ratio $a/b = 8$ (see Fig. 1). In principle, larger sensors are favorable for better resolution. The chosen dimensions are determined according to the capability to fabricate large ellipses without any detrimental imperfections. Accordingly, we have fabricated sensors with $a = 3$ mm. The distance d between the current leads should be as small as possible to decrease the resistance R_x. On the other hand, if the leads are too close a significant part of the current would flow through V_y leads instead of flowing through the magnetic layer which would decrease significantly the PHE signal. Therefore, we chose $d = 1.2$ mm and $d/e = 20$.

The sensor parameters are listed in Table 1. The values of $\Delta\rho/\rho$, ρ, and H_a were determined by measurements as described in Mor [2012].

The sensor was excited with ac current. The sensor output was amplified using a low-noise operational amplifier (LT1028). The amplifier output was sampled by a 24-bit ADC (PXI-5421) and demodulated using a digital synchronous detector. A 100-Hz low-pass filter at the output of the synchronous detector was used to band limit the signal.

As the input voltage noise of the LT1028 operational amplifier flattens at around 1 kHz, we have excited the sensor at 1.22 kHz to avoid the amplifier $1/f$ noise and 50-Hz power network harmonics.

Table 1. Parameters of the optimized PHE sensor experimental model.

Parameter	Value	Units	Parameter	Value	Units
a	3	mm	H_a	3.84	Oe
b	0.375	mm	H_k	3.45	Oe
t	120	nm	$\Delta\rho/\rho$	1.6	%
d	1.2	mm	ρ	$2.7\ 10^{-7}$	Ohm·m
e	0.06	mm	α	1.5	
R_x	9.97	Ohm	δ_H	$2.73\ 10^{-3}$	
R_y	5.08	Ohm	N_c	$17\ 10^{28}$	$1/m^3$
I_x	71.4	mA			

The sensor gain S_y was measured using a calibrated solenoid and was found to be flat from 10 mHz to 100 Hz.

The sensor noise was measured by using a seven layer magnetic shield to suppress low-frequency interferences. To find the optimal excitation current, we have changed it by small steps measuring at each step the sensor gain and noise.

Theoretically, if the sensor power consumption is not limited, the excitation current should be as high as possible to bring the equivalent magnetic noise to a minimum at all frequencies. However, the ability of the sensor to dissipate the excessive heat is limited and, therefore, at a too high current, the sensor becomes thermally unstable, which degrades its equivalent magnetic noise.

From measurements of R_x, we have found $C_1 = 1.38$ according to (8), where ρ, d, t, and b are known. To find $C_2 = 4.23$, we have simulated with COMSOL software R_y according to (10), where $C_3 = 1$, because the simulation does not consider the interface resistance between the gold and Permalloy films. Then by substituting C_2 into (10) and comparing it to the measured value of R_y, we have determined $C_3 = 1.53$.

Fig. 3 shows the sensor equivalent magnetic noise for the case of too low (35.7 mA), optimal (71.4 mA), and too high (83.3 mA) excitation currents, I_x.

The measured equivalent magnetic noise in nT/$\sqrt{\text{Hz}}$ is fitted as follows:

$$B_{\text{eq}} = a_0 + a_1 \cdot \frac{1}{f^{0.75}} \quad (15)$$

with $a_0 = 0.83$ and $a_1 = 0.14$ for $I_x = 35.7$ mA; $a_0 = 0.4$ and $a_1 = 0.17$ for $I_x = 71.4$ mA; $a_0 = 0.35$ and $a_1 = 0.24$ for $I_x = 83.3$ mA.

One can see from Fig. 3 that the sensor equivalent magnetic noise at the optimal excitation current is either the lowest one or does not practically differ from the noise values at the other excitation currents. A too low excitation current provides similar results at low frequencies but worse results at higher frequencies, where the $1/f$ noise is not so dominant. At a too high excitation current, the equivalent magnetic noise at high

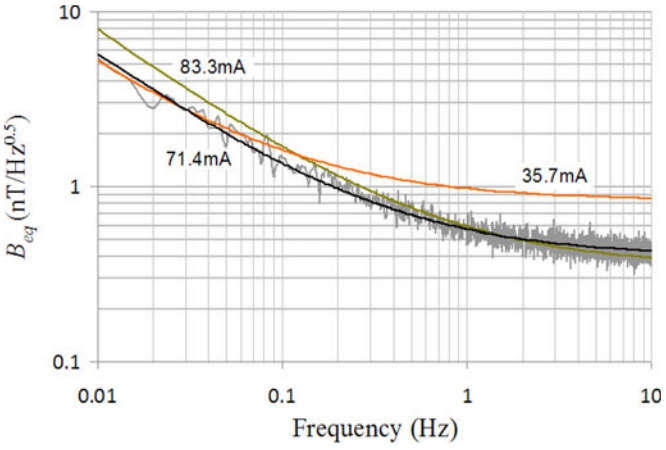

Fig. 3. Equivalent magnetic noise versus frequency. For the optimum excitation current amplitude of 71.4 mA, both the sensor noise and the noise fit are shown. For other excitation current amplitudes only the noise fits are shown.

frequencies is similar to that of the optimal current, but is degraded at low frequencies due to thermal drift.

From the obtained results for the optimal current, we estimate the Hooge constant $\delta_H = 2.73 \times 10^{-3}$. This value differs only by 36% from the so called "Hooge magic number" of 2×10^{-3} which was vastly reported as the Hooge constant for single layer metal films in general [Ziese 2001], and magnetic films in particular [Gijs 1997].

We have built and tested three additional identical sensors and have found that their noise and sensitivity do not differ by more than 10% from the sensor described previously.

The white noise components, e.g., thermal and preamplifier noise, degrades the sensor optimal equivalent magnetic noise by 40% at 0.1 Hz, 300% at 1 Hz, and more than 1000% at 10 Hz. Although our preamplifier has a very low noise of 1 nV/$\sqrt{}$Hz, it is still three times larger than the thermal noise of the sensor (0.29 nV/$\sqrt{}$Hz). Therefore, we expect a significant improvement in the equivalent magnetic noise by using a lower noise preamplifier [Levinzon 2008], especially at higher frequencies. Further improvement in the equivalent magnetic noise is possible due to the following. The highest $\Delta\rho/\rho$ value for our sensors is about 1.6%, which may be increased up to 4% by using an insulation layer, consisting of a thermal silicon dioxide or a low stress silicon nitride deposited by a PECVD process at low temperatures [Hauser 2000]. Ferromagnetic nitride films exhibiting $\Delta\rho/\rho$ on the order of 6% [Loloee 2012] can also be considered. Increasing $\Delta\rho/\rho$ by a factor of 2 and decreasing H_a by a factor of 5 [Loloee 2012] is expected to improve the equivalent magnetic noise by a factor of 4.5.

V. CONCLUSION

By exciting the sensor with an optimized ac current and optimizing the sensor thickness, we have decreased the sensor $1/f$ noise drastically and improved its resolution at low frequencies. The obtained resolution 570 pT/$\sqrt{}$Hz at 1 Hz, is 3.5 times better than the best results [Persson 2013] reported for the PHE sensors. From 0.2 Hz and below, it is also better than the resolution of the best AMR sensors [Stutzke 2005, Honeywell 2008].

ACKNOWLEDGMENT

This work was supported in part by Analog Devices, Inc. Authors A. Grosz and V. Mor contributed equally to this work.

REFERENCES

Ejsing L W (2006), *Magnetic Beads in Microfluidic Systems*, Ph.D. thesis, Technical University of Denmark, Lyngby, Denmark.

Gijs M A M, Giesbers J B, Beliën P, van Est J W, Briaire J, Vandamme L K J (1997), "1/f noise in magnetic $Ni_{80}Fe_{20}$ single layers and $Ni_{80}Fe_{20}$/Cu multilayers," *J. Magn. Magn. Mater.*, vol. 165, pp. 360–362, doi: 10.1016/S0304-8853(96)00555-0.

Hauser H, Stangl G, Hochreiter J (2000), "High-performance magnetoresistive sensors," *Sensors Actuators A*, vol. 81, pp. 27–31, doi: 10.1016/S0924-4247(99)00165-X.

Honeywell (2008), "1- and 2-axis magnetic sensors HMC1001/1002/1021/1022," Honeywell International Inc. Available: http://www51.honeywell.com/aero/common/documents/myaerospacecatalog-documents/Missiles-Munitions/HMC_1001-1002-1021-1022_Data_Sheet.pdf.

Hu J, Tian W, Zhao J, Pan M, Chen D, Tian G (2013), "Remedying magnetic hysteresis and 1/f noise for magnetoresistive sensors," *Appl. Phys. Lett.*, vol. 102, 054104, doi: 10.1063/1.4790606.

Lei Z Q, Li G J, Egelhoff W F, Lai P T, Pong P W T (2011), "Review of noise sources in magnetic tunnel junction sensors," *IEEE Trans. Magn.*, vol. 47, pp. 602–612, doi: 10.1109/TMAG.2010.2100814.

Levinzon F A (2008), "Ultra-low-noise high-input impedance amplifier for low-frequency measurement applications," *IEEE Trans. Circuits Syst.-I*, vol. 55, pp. 1815–1822, doi: 10.1109/TCSI.2008.918213.

Liou S H, Yin X, Russek S E, Heindl R, Da Silva F C S, Moreland J, Pappas D O, Yuan L, Shen J (2011), "Picotesla Magnetic Sensors for Low-Frequency Applications," *IEEE Trans. Magn.*, vol. 47, pp. 3740–3742, doi: 10.1109/TMAG.2011.2157997.

Loloee R (2012), "Epitaxial Ni_3FeN thin films: A candidate for spintronic devices and magnetic sensors," *J. Appl. Phys.*, vol. 112, 023902, doi: 10.1063/1.4737407.

Montaigne F, Schuhl A, Nguyen Van Dau F, Encinas A (2000), "Development of magnetoresistive sensors based on planar Hall effect for applications to microcompass," *Sens. Actuat. A*, vol. 81, pp. 324–327, doi: 10.1016/S0924-4247(99)00102-8.

Mor V, Schultz M, Sinwani O, Grosz A, Paperno E, and Klein L (2012), "Planar Hall effect sensors with shape-induced effective single domain behavior," *J. Appl. Phys.*, vol. 111, 07E519, doi: 10.1063/1.3680084.

Nemoto A, Otani Y, Kim S G, Fukamichi K, Kitakami O, Shimada Y (1999), "Magnetoresistance and planar Hall effects in submicron exchange-coupled NiO/Fe19Ni81 wires," *Appl. Phys. Lett. A*, vol. 74, pp. 4026–4028, doi: 10.1063/1.123249.

Persson A, Bejhed R S, Østerberg F W, Gunnarsson K, Nguyen H, Rizzi G, Hansen M F, Svedlindh P (2013), "Modelling and design of planar Hall effect bridge sensors for low-frequency Applications," *Sensors and Actuators A*, vol. 189, pp. 459–465, doi: 10.1016/j.sna.2012.10.037.

Ripka P, Janošek M (2010), "Advances in agnetic ield ensors," *IEEE Sensors J.*, vol. 10, pp. 1108–1116, doi: 10.1109/JSEN.2010.2043429.

Schuhl A, Nguyen Van Dau F, Childress J R (1995), "Low-field magnetic sensors based on the planar Hall effect," *Appl. Phys. Lett.*, vol. 66, pp. 2751–2753, doi: 10.1063/1.113697.

Stutzke N A, Russek S E, Pappas D P, Tondra M (2005), "Low-frequency noise measurements on commercial magnetoresistive magnetic field sensors," *J. Appl. Phys.*, vol. 97, 10Q107, doi: 10.1063/1.1861375.

Ziese M, Thornton M J (2001), *Lecture Notes in Physics*. Berlin, Germany: Springer-Verlag, p. 569.

Composed planar Hall effect sensors with dual-mode operation

Vladislav Mor, Debangsu Roy, Moty Schultz, and Lior Klein
Department of Physics, Nano-magnetism Research Center, Institute of Nanotechnology and Advanced Materials, Bar-Ilan University, Ramat-Gan 52900, Israel

(Received 12 November 2015; accepted 27 January 2016; published online 4 February 2016)

We present a composed planar Hall effect sensor with two modes of operation: (a) an ON mode where the composed sensor responds to magnetic field excitations similarly to the response of a regular planar Hall effect sensor, and (b) an OFF mode where the response is negligible. The composed planar Hall effect sensor switches from the OFF mode to the ON mode when it is exposed to a magnetic field which exceeds a certain threshold determined by the sensor design. The features of this sensor make it useful as a switch triggered by magnetic field and as a sensing device with memory, as its mode of operation indicates exposure to a magnetic field larger than a certain threshold without the need to be activated during the exposure itself. [http://dx.doi.org/10.1063/1.4941694]

I. INTRODUCTION

Commonly magnetic sensing devices and magnetic memory devices are distinct: magnetic sensing devices respond reversibly to magnetic field excitations without any history effects, while magnetic memory devices store the most recent WRITE operation. Here, we present a device that combines sensing and memory properties: a composed planar Hall effect sensor (CPHES) with dual mode operation. The CPHES has two modes of operation: an ON mode where the response of the CPHES is similar to the response of a regular planar Hall effect sensor (PHES) and an OFF mode where the response of the CPHES is negligible. The CPHES switches from an OFF mode to an ON mode when it is exposed to a magnetic field exceeding a certain threshold value determined by the fabrication parameters of the CPHES.

The operation of the CPHES is based on the planar Hall effect (PHE)[1] in polycrystalline ferromagnetic films. Due to this effect, in magnetic films parallel to the xy plane with in-plane magnetization $\mathbf{M}$, a current density in the x direction (J_x) gives rise to a transverse electric field in the y direction (E_y). The resulting transverse resistivity ρ_{xy} given by E_y/J_x is determined by the angle θ between J_x and $\mathbf{M}$ as follows:

$$\rho_{xy} = \frac{1}{2}(\rho_{\parallel} - \rho_{\perp}) \sin 2\theta, \tag{1}$$

where $\rho_{\parallel}$ and $\rho_{\perp}$ are the resistivities over directions parallel and perpendicular to $\mathbf{M}$, respectively. PHE magnetic sensors[2–8] based on such magnetic films commonly have an easy axis of magnetization parallel to the current flow, which yields zero ρ_{xy} when the external magnetic field is zero. When a magnetic field perpendicular to the easy axis is applied, the magnetization rotates reversibly away from the easy axis and the measured ρ_{xy} indicates the external magnetic field.

PHE sensors based on elongated magnetic ellipses made of Permalloy exhibit shape-induced magnetic anisotropy along the long axis.[9–12] The ellipses are shown to have effective single magnetic domain behavior and in the limit of $a \gg b \gg t$ the magnitude of the anisotropy field H_k is reliably determined by

$$H_k \simeq 4\pi M_s \frac{t}{b} \simeq 10,807 \frac{t}{b} \text{ Oe}, \tag{2}$$

where a, b and t are the ellipse's long axis, short axis, thickness, respectively, and M_s is the saturation magnetization. As demonstrated before, these PHE sensors exhibit excellent magnetic field resolution.[12]

The CPHES presented here is based on a pair of elongated magnetic ellipses made of Permalloy (see Figure 1), and the PHE response is measured across the two ellipses. As we show, parallel magnetization alignment in the two ellipses, corresponding to an ON mode, yields a PHE response similar to a response of a single PHE ellipse, while antiparallel magnetization alignment, corresponding to an OFF mode, yields a negligible response. We also show switchings between OFF and ON modes of a CPHES triggered by magnetic field.

The CPHES can be useful for a variety of applications. It can be used as a switch triggered by magnetic field. It can be used as a marker which indicates exposure to a magnetic field exceeding a certain threshold without the need to constantly monitor the magnetic field. In addition, it can be used as a sensing device sampled at a low rate before a triggering event, and once it is activated it can be used as a sensitive magnetic field sensor sampled at a higher rate.

II. DEVICE MANUFACTURING AND EXPERIMENTAL SETUP

To fabricate the CPHES, we sputter Permalloy ($Ni_{80}Fe_{20}$) films capped with tantalum on Si substrates in a UHV sputtering system (BESTEC). We pattern the pairs of ellipses with MJB4 Mask Aligner using lift-off. Gold leads and contact pads are deposited in the second stage.

Figure 1 presents the structure of the CPHES. It is composed of two magnetic ellipses made of Permalloy ($Ni_{80}Fe_{20}$) placed in parallel to each other. Current is driven in parallel through the ellipses and the transverse voltage is measured across both ellipses. The dimensions of the ellipses are 1 mm long, 0.125 mm wide, and 60 nm thick, and the current **I** is applied along the long axis of the two ellipses. The distance between the centers of the two ellipses is 225 μm. For this distance, the magnetostatic interaction between the ellipses is negligible. Due to symmetry considerations, the average stray field in the sensing direction (H_y) that one ellipse generates on the other ellipse is zero and its maximum absolute value is found to be 0.25 Oe. The stray field component along x and z direction are smaller than 0.1 Oe and 5e-5 Oe, respectively. The home-built measuring system consists of two pairs of Helmholtz coils which produce magnetic fields perpendicular to each other. The device is placed on a rotating stage with an angle resolution of 0.03°. The sample is connected electrically to a switch box (Keithley 7001), a current source (Keithley 2400), and a nanovoltmeter

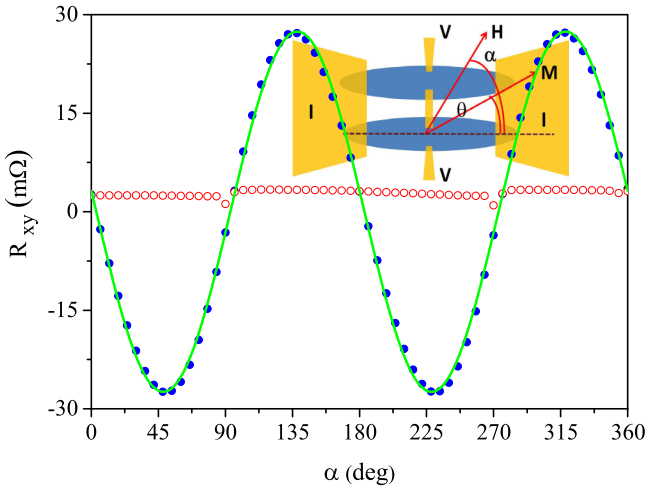

FIG. 1. R_{xy} measured across the CPHES as a function of the angle α between **H** and **I**. For each angle α, the resistance is measured twice: with $H = 100$ Oe (filled blue symbols) and with $H = 0$ (unfilled red symbols). The solid line is a fit to Eq. (1). Inset: A sketch of a typical CPHES. The elliptical part is made of Permalloy capped with tantalum. Current is applied via the **I** contact pads and the output voltage is measured at the **V** contact pads.

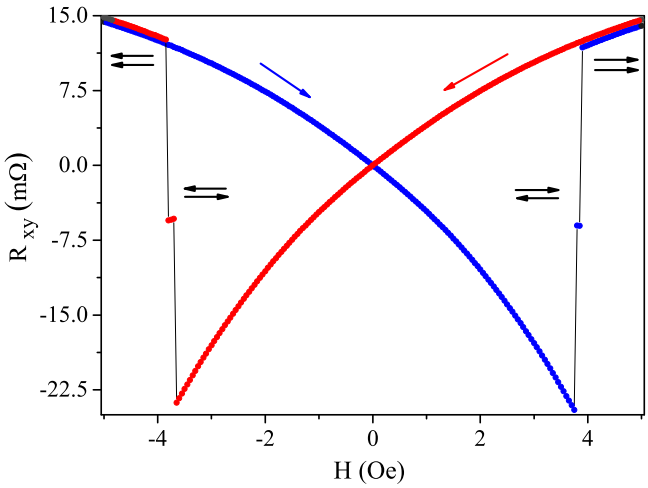

FIG. 2. Hyteresis loop of R_{xy} of a CPHES device as a function of a magnetic field applied at 45° relative to the long axis of the ellipses. The relative orientation of the magnetization in different parts of the loop is indicated.

(Keithley 2182). The two pairs of Helmholtz coils are connected to two current sources (Keithley 2420 and Keithley 2425).

III. RESULTS AND DISCUSSION

Figure 1 shows $R_{xy} = V_y/I_x$ of the CPHES (V_y is the voltage measured across the CPHES and I_x = 2.5 mA is the current driven through the CPHES) as a function of the angle (α) between an applied magnetic field of 100 Oe and the current. For this field **M** is parallel to **H**; hence, $\alpha = \theta$ (manifested in the fit to Eq.(1) in Fig. 1). At each angle, R_{xy} is measured twice with a field and then after removing the field. The data confirm that as shown previously for a single ellipse,[11] when the applied magnetic field is set to zero, the magnetization fully returns to its orientation along the shape-induced easy axis.

Figure 2 shows R_{xy} as a function of **H** applied at $\alpha = 45°$. At sufficiently high fields (positive or negative) the two ellipses are magnetically parallel. However, we note that the switching occurs in two steps; namely, there is a narrow window of fields where only one of the ellipses has switched. It means that we can prepare the ellipses in four different remanent states: parallel **M** in the negative or positive direction, and two antiparallel **M** states. Although the field interval for inducing the antiparallel states is quite narrow, the procedure is reproducible and once the antiparallel state is induced, it remains stable when the field is set to zero. Namely, the remanent antiparallel states are stable. Figure 3 shows the response of the CPHES in four corresponding remanent states for **H** applied at $\alpha = 45°$.

Figure 4 demonstrates switching behavior of the CPHES between the two modes in a response to a DC magnetic field ($\alpha = 135^o$). The device is prepared in an antiparallel **M** state by applying an appropriate sequence of magnetic fields, as demonstrated in Figure 2. Subsequently, the field is set to zero so that the device is in a remanent antiparallel **M** state. This is the starting point of the experiment shown in Figure 4. We then gradually increase a DC field applied at $\alpha = 135^o$ and measure the response of the CPHES to a small AC magnetic field (±0.1 Oe) which is perpendicular to the DC magnetic field. At low fields the response is negligible; hence, we name this state the OFF mode. After switching, the response is much larger; hence, we call this state the ON mode. The switching from OFF to ON is irreversible, and when the field is decreased below the switching field the CPHES remains in the ON mode. To set the OFF mode one needs to apply the process described above.

The switching behavior of the CPHES shows that the CPHES can be used as a switch or a fuze triggered by magnetic field. It should be noted that the triggering fields can be tailored by the geometrical parameters of the ellipse, as demonstrated before for a single ellipse.[11]

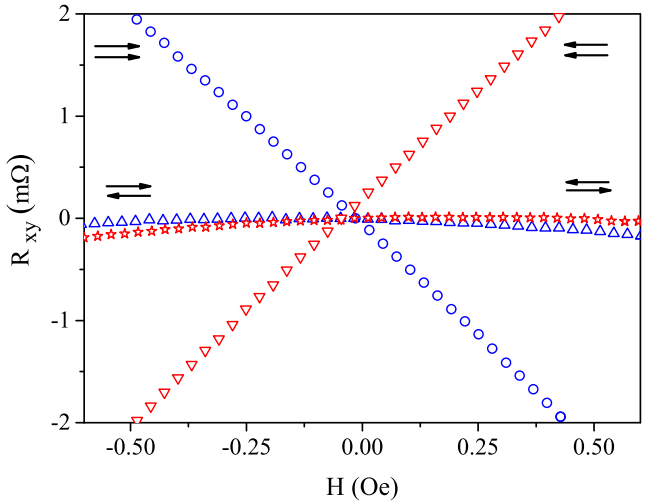

FIG. 3. Low-field response of the CPHES in four different remanent states.The corresponding magnetization configurations of four different remanent states are depicted in the figure.

Another potential application is for two modes of surveillance. Movement of objects containing magnetic materials cause disturbances in the magnetic field which can be picked by magnetic sensors.[13] An important issue for operating a large number of magnetic sensors spread over different environments (e.g., for smart dust applications)[14] is power consumption. If CPHES are used for such applications, they can be probed at a certain rate as long as they are in an OFF state and at a different rate after they are switched to an ON state, thus conserving the energy.

The fact that the CPHES store information on fields to which it was exposed may be useful in cases where it is important to know the magnetic fields to which an object was exposed when it is impossible or inconvenient to measure such magnetic field in real time.

Here we show CPHES where the two ellipses are next to each other. In principle, the CPHES can be made with the two ellipses on top of each other separated by a non-magnetic spacer (see inset of Figure 5). In addition , the latter structure may have other advantages. In the OFF state the stray field at the edges of the ellipses is much smaller than the stray field in the ON state. Figure 5 shows

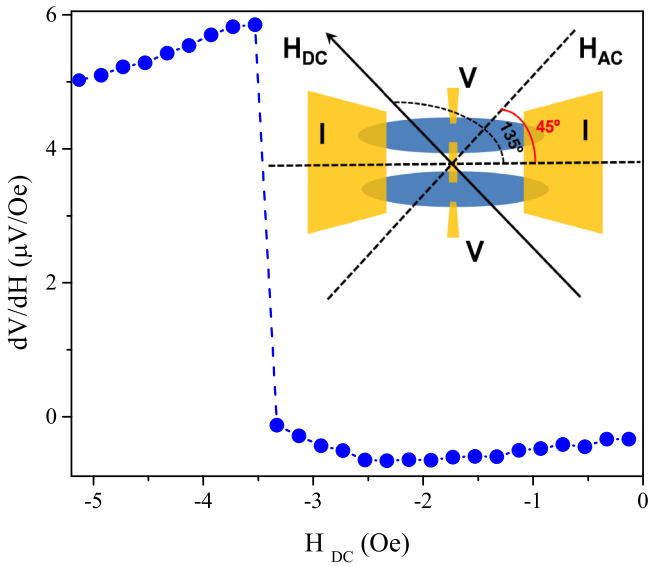

FIG. 4. The response of the CPHES to an AC field as a function of the DC field. The DC field is applied at $\alpha = 135^{o}$ and the AC field is perpendicular to it and both of them lie in the plane of the CPHES.

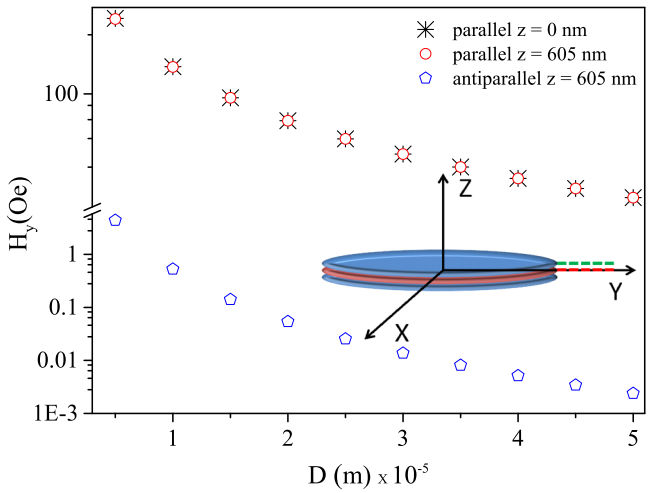

FIG. 5. The calculated stray field as a function of the distance from the a CPHES (a = 5 mm b = 0.625 mm c = 600 nm) considering the parallel and antiparallel configuration of the magnetization on the green line whereas for the red line; the magnetization is in the antiparallel state. Inset: the CPHES with the two ellipses on top of each other with a non-magnetic spacer. The red dashed line is parallel to the long axis of the ellipse and starting on the edge of the spacer between the two Permalloy ellipses (z = 0 nm). The green dashed line is parallel to the long axis of the ellipse and starting on the top edge of the CPHES (z = 605 nm).

the calculated stray field distribution on two lines starting at the edge of the CPHES and parallel to the Y axis: z = 0nm (red dashed line) and z = 605 nm (green dashed line). For the red dashed line, D = 0 is the edge of the spacer between the two Permalloy ellipses, while for the green dashed line D = 0 is the top edge of the CPHES. This feature enables a visual read of the CPHES mode. For example, magnetochromatic materials[15–17] placed near the edges of the device can provide a visual indication. Today's magnetochromatic materials need at least tens of oersted to give a noticeable color change, so we need to use bigger CPHES in order to obtain a sufficiently large magnetic field. Using such a configuration the CPHES can be used without any electronics similarly to the way tilt or shock indicators are used for parcels. This may be useful for shipments sensitive to magnetic fields: cards with encoded magnetic information (e.g., credit cards), magnetic memory devices, etc. CPHES may also be used in arrays with a distribution of the orientation of easy axis and the magnitude of the anisotropy field. Such arrays will enable the determination of an upper bound and not only a lower bound for the magnetic field. In addition it will provide information on the orientation of the field to which the CPHESs were exposed.

IV. SUMMARY

We have designed and fabricated a composed PHE magnetic sensor and demonstrated its features. The new proposed device may be used in wide range of applications like smart dust, or magnetic fuze, or magnetic indicators.

ACKNOWLEDGMENTS

L.K. acknowledges support by the Israel Science Foundation founded by the Israel Academy of Science and Humanities.

[1] C. Goldberg and R. E. Davis, Phys. Rev. **94**, 1121 (1954).
[2] F. G. West, J. Appl. Phys. **34**, 1171 (1963).
[3] A. Schuhl, F. N. Van Dau, and J. R. Childress, Appl. Phys. Lett. **66**, 2751 (1995).
[4] C. D. Damsgaard, B. T. Dalset, S. C. Freitas, P. P. Freitas, and M. F. Hansen, Sensors and Actuators A **56**, 103 (2009).
[5] A. Nemoto, Appl. Phys. Lett. **74**, 4026 (1999).
[6] T. Q. Hung, S. Oh, J. Jeong, and C. Kim, Sensors and Actuators A **157**, 42 (2010).

[7] T. Q. Hung, S. Oh, B.l Sinha, J. Jeong, D. Kim, and C. Kim, J. Appl. Phys. **107**, 09E715 (2010).
[8] S. J. Oh, Tuan Tu Le, G. W. Kim, and Cheo Gi Kim, physica status solidi (a) **204**(12), 4075 (2007).
[9] C. C. Chang, Y. C. Chang, W. S. Chung, J. C. Wu, Z. H. Wei, M. F. Lai, and C. R. Chang, IEEE TRANSACTIONS ON MAGNETICS. **41**(2), 947 (2005).
[10] I. Genish1, Y. Shperber, N. Naftalis, G. Salitra, D. Aurbach, and L. Klein, J. Appl. Phys. **107**, 09E716 (2010).
[11] V. Mor, M. Shultz, O. Sinwani, A. Grosz, E. Paperno, and L. Klein, J. Appl. Phys. **111**, 07E519 (2012).
[12] A. Grosz, V. Mor, E. Paperno, S. Amrusi, I. Faivinov, M. Schultz, and L. Klein, IEEE MAGNETICS LETTERS. **4**, 6500104 (2013).
[13] K. Finkenzeller, John Wiley, Ltd, New York, 19, 2010.
[14] K. Finkenzeller, Proceedings of the IEEE **94**(6), 1177 (2006).
[15] J. Ge, H. Lee, L. He, J. Kim, Z. Lu, H. Kim, J. Goebl, S. Kwon, and Yadong Yin, J. Am. Chem. Soc. **131**(43), 15687 (2009).
[16] L. Zhuang, W. Zhang, Y. Zhao, H. Shen, H. Lin, and J. Liang, Scientific Reports **5**, 9320 (2015).
[17] L. He, M. Janner, Q. Lu, M. Wang, H. Ma, and Y. Yin, Adv. Matter **27**, 86 (2015).

תקציר

בעידן המודרני, חיישנים רגישים לגילוי של שדה מגנטי הם חלק בלתי נפרד מהחיים שלנו. הם משמשים אותנו לקריאה של התקני זכרון מגנטי, לגילוי שינויים בשדה מגנטי של כדור הארץ לצורכי ניווט או לגילוי חפצים הכוללים בתוכם חומרים מגנטיים, לחישה של הפרש פוטנציאלים או הזזה בתדירות, תהודה מגנטית, וכד'. בין הסוגים השונים של החיישנים המגנטיים, מעניינים במיוחד החיישנים המבוססים על האניאיזוטרופיה של ההתנגדות המגנטית Aanisotropic magneto resistance) AMR) וזאת הודות לרגישותם הגבוהה ומחירם הזול. מסיבות אלה משתמשים בהם במגוון רחב של תחומי התעשייה והטכנולוגיה וכן בחיי היום-יום. על כל פנים עדיין קיימים תחומים חשובים כמו יישומים רפואיים ובטחונים שעבורם הרגישות הקיימת אינה מספיקה. מסיבה זו פיתוח דרכים חדשות לייצור חיישני AMRיחסית זולים, פשוטים ורגישים שמסוגלים לפעול בטמפרטורת החדר היא מטרה חשובה ואטרקטיבית.

בתזה זו, אנחנו מדגימים את הפוטנציאל של חיישני שדה מגנטיים אולטרה-רגישים, המבוססים על אפקט הול המשטחי ((Planar Hall Effect (PHE) בשכבות של פרמלוי ((Permalloy(Py). החיישן המתואר בעבודה זו מנצל את העיקרון של האניזוטרופיה המגנטית המושרת על ידי צורה. החיישן מותאם להשגת אות גדול ורעש נמוך. כתוצאה מכך, רזולוציית השדה היא בסדר גודל גבוה יותר מכל תוצאה אחרת שדווחה עבור חיישן PHE. יתר על כן, בתדרים נמוכים הוא רגיש יותר מכל חיישן AMR מסחרי ידוע.

המאמר הראשון "Planar Hall effect sensors with shape-induced effective single domain behavior" [I] מציג מחקר מקיף של אניזוטרופיה המגנטית המושרת על ידי צורה בשכבות דקות של Permalloy בדוגמאות בצורת אליפסות מוארכות. חקרנו אליפסות במגוון רחב של גדלים: מאליפסות קטנות בסדר גודל של מיקרומטרים ועד אליפסות של מילימטרים בודדים. הראינו כי אניזוטרופיה צורנית יכולה לשמש באופן מהימן להשגה של התנהגות של דומיין מגנטי בודד. תופעה זו קיימת גם באליפסות עם ציר ראשי מסדר מילימטרי, בתנאי שיחס הצירים של האליפסות הוא גדול מספיק. אנחנו גם הראנו כי ניתן לחשב אנליטית את האיזוטרופיה הצורנית. בנוסף למודל אנליטי, ביצענו סימולציות נומריות באמצעות תוכנת OOMMF. עבור אליפסות ואליפסואידים

הסימולציות הצביעו על התנהגות אפקטיבית של דומיין מגנטי בודד וזאת בתחום רחב של הגדלים. לעומת זאת, דגימות מלבניות הן פחות יציבים. מחקר זה פותח את הדלת לשימוש באליפסות בתור חלק מרכזי של חיישנים מגנטים מבוססי PHE.

המאמר השני " Planar Hall Effect Sensors With Subnanotesla Resolution " [II] מציג את מודל הרעש של החיישן. זיהינו את הגורמים המשפיעים על הרעש ופיתחנו מודל לרעש וכך הצלחנו לעשות אופטימיזציה לתכונות החיישן ולהגיע לרגישות של $600\ ^{pT}/_{\sqrt{Hz}}$. המודל שלנו לוקח בחשבון מקורות שונים של רעש: רעש מגבר, רעש תרמי ורעש $1/f$. כדי לפתח חיישני PHE עם רזולוציה משופרת, נקטנו בצעדים הבאים: (א) השתמשנו בזרם ערור AC בכדי לתרגם את אות היציאה של החיישן לתדירויות ששם אפשר להזניח את רעש $1/f$ ואת רעש של המגבר. ביצענו את ההתאמה של עובי השכבה לפי המודל האנליטי, הקטנו את שדה האניזוטרופיה וזאת כדי להגדיל את הרגישות של החיישן.

המאמר השלישי " Composed planar Hall effect sensors with dual-mode operation " [III] דן באחד מיני רבים יישומים אפשריים: התקן המשלב תכונות חישה וזיכרון. במאמר הצגנו חיישן אפקט הול מישוריים מורכב (CPHES) עם שני מצבי פעולה.CPHES מבוסס על זוג אליפסות מגנטיות מוארכות עשויות Permalloy, ותגובת PHE נמדדת על פני שתי האליפסות. כיוון מקביל של המגנטיזציה בשתי אליפסות, מתאים למצב ON, מניב תגובת PHE דומה לתגובה של אליפסה PHE אחת, בעוד שכיוון המגנטיזציה אנטי מקביל (antiparallel) , מתאים למצב OFF, מניב תגובה זניחה.

הראינו מעברים בין המצבים השונים של ה CPHES המופעלים על ידי שדה מגנטי. עבור התקן זה, ניתן לחשוב על מגוון רחב של יישומים: מתג המופעל על ידי שדה מגנטי, סמן המצביע על חשיפה לשדה מגנטי העולה על סף מסוים ללא הצורך לדגום את השדה המגנטי כל הזמן. החידוש כאן הוא שניתן להתאים את שדה ההפעלה על ידי בחירה של יחס צירים של האליפסות.

בנוסף למחקר העיקרי שתואר לעיל, היינו יכולים לתרום תרומה חשובה למחקר הקשור לזיכרון מגנטי בגישה אקראית (MRAM) [VIII-VI] המבוסס על אפקט הול משטחי. שלושה מאמרים בנושא זה מוצגים בסעיף הפרסומים. בנוסף, שיתפנו פעולה עם קבוצה במחלקה לכימיה בחקר של צינורות-ננו-פחמן (CNT) [IX].

לסיכום, ההישג העיקרי של המחקר שלנו הוא הפיתוח של חיישן מגנטי אולטרה רגיש מבוסס על PHE אשר רגיש ביותר מסדר גודל מכל חיישן PHE אחר, ובתדרים נמוכים אף רגיש יותר מכל חיישן AMR מסחרי ידוע. הישג זה פותח את הדלת עבור יישומים רבים בתחומים שונים, כולל יישומים צבאיים ורפואיים.

אנו מייחסים את הרגישות יוצאת דופן של החיישנים שלנו למספר גורמים: (א) לימוד ופיתוח השימוש באנאיזוטרופיה צורנית, השראת האניזוטרופיה על ידי הגדרת הצורה האליפטית של החיישן (ב) פיתוח מודל רעש ושימוש בו לאופטימיזצית ממדי החיישן (ג) אופטימיזציה של תהליך הייצור הכולל נידוף השכבות והליתוגרפיה.

בהתבסס על הבנתנו הנוכחית של הגורמים החשובים הקובעים את רגישות החיישן, אנו בטוחים כי ניתן לשפר עוד יותר את רזולוציית השדה וזאת לפחות בסדר גודל אחד. שיפור זה יהפוך את החיישנים שלנו עוד יותר אטרקטיביים עבור יישומים שונים. כעת בקבוצה שלנו, מנסים לפתח מערכת מעבדה-על-שבב שנועדה לזהות ריכוזים קטנים מאוד של חלבונים ספציפיים בתמיסה .שיטת זיהוי מבוססת על שימוש בחיישנים מגנטיים על מנת לזהות את המאפיינים ההידרודינמים של חלקיקים מגנטיים המצופים חומר מיוחד הגורם לחלבונים הספציפיים להתחבר אליהם. התנועה הבראונית של החלקיקים המגנטיים משתנה כאשר חלבונים נקשרים אליהם וניתן לראות שינויים אלו בתגובת החיישן. אנו מאמינים שזו רק ההתחלה ו יגיעו עוד יישומים עם שיפור נוסף של החיישנים.

תוכן עניינים:

עבודה זו נעשתה בהדרכתו של

פרופ' ליאור קליין

מן המחלקה לפיסיקה

של אוניברסיטת בר-אילן.

תכונות פיסיקליות הקובעות את גבול הרזולוציה של סנסורים מבוססי אפקט הול משטחי

חיבור לשם קבלת התואר "דוקטור לפילוסופיה"

מאת:

ולדיסלב מור

המחלקה לפיסיקה

הוגש לסנט של אוניברסיטת בר-אילן

רמת גן טבת תשע"ו